AGU PUBLICATIONS

Tectonics

RESEARCH ARTICLE
10.1002/2015TC004101

Key Points:
- We analyze the accretion of foreland basin sediments during early stages of continental collision
- The tectonic style is largely controlled by the diagenetic state of the sediments
- The overall tectonics are similar to the one of accretionary wedges

Supporting Information:
- Supporting Information S1

Correspondence to:
A. Dielforder,
armin@crpg.cnrs-nancy.fr

Citation:
Dielforder, A., A. Berger, and M. Herwegh (2016), The accretion of foreland basin sediments during early stages of continental collision in the European Alps and similarities to accretionary wedge tectonics, *Tectonics*, *35*, 2216–2238, doi:10.1002/2015TC004101.

Received 6 DEC 2015
Accepted 6 AUG 2016
Accepted article online 9 AUG 2016
Published online 6 OCT 2016

The accretion of foreland basin sediments during early stages of continental collision in the European Alps and similarities to accretionary wedge tectonics

Armin Dielforder[1], Alfons Berger[1], and Marco Herwegh[1]

[1]Institute of Geological Sciences, University of Bern, Bern, Switzerland

Abstract We present structural observations from foreland basin sediments that were incorporated into the orogenic wedge of the central European Alps during early stages of continental collision. Our analysis focuses on the prograde evolution and considers the full history of the sediments ranging from their deposition in the basin to deep burial and metamorphism at temperatures of ~320°C. The tectonic evolution is matched with constraints on the diagenetic alteration of the sediments. For this purpose, we calculate the temperatures and depths of sediment compaction and illitization as well as the associated fluid liberation. The data set highlights that the tectonic incorporation of the sediments into the orogenic wedge was strongly controlled by their diagenetic state. Earliest deformation took place during imbrication and frontal accretion of unconsolidated and fluid-saturated sediments. Ductile folding of the sediments occurred already at this stage and was assisted by particulate flow. With the progressive consolidation of the sediments the elastic strength increased, which resulted in an overall embrittlement. This rheological change is recorded by the onset of out-of-sequence thrusting, brittle faulting, and the formation of massive quartz-calcite veins, which took place in the approximate temperature range of the seismogenic zone (i.e., ~150–350°C). Moreover, widespread pressure solution resulted in the formation of a penetrative cleavage and records slow but long-lasting deformation at low background strain rates. In summary, the prograde tectonic evolution of the frontal Alpine wedge exhibits many similarities with the structural and mechanical evolution of accretionary wedges at active subduction zones.

1. Introduction

Peripheral foreland basins are a major element in the tectonic framework of collisional orogens [e.g., *Beaumont,* 1981; *Allen et al.,* 1986]. They form during the closure of an oceanic basin and the subsequent collision of a passive margin with an island arc or active continental margin. The sedimentary record and geometry of foreland basins are commonly used to reconstruct the evolution of collisional orogens through time and space [e.g., *Sinclair et al.,* 1991; *Pelletier*, 2007]. This is because the basin shape is thought to be at first order a function of the flexural rigidity of the lower plate and therefore related to the load induced by the thrust wedge and basin sediments [e.g., *Jordan*, 1981]. Moreover, facies changes and basin migration were used to determine rates of wedge exhumation, erosion, or thrust wedge advance [e.g., *Sinclair and Allen*, 1992]. More recently, other crustal- to lithospheric-scale processes that potentially control the evolution of foreland basins were recognized. For example, slab pull, slab breakoff, and slab rollback were suggested to affect the subsidence of forelands basins [e.g., *Sinclair*, 1997b; *Garcia-Castellanos and Cloetingh*, 2012; *Schlunegger and Kissling*, 2015]. Similarly, the accommodation of slip across a major range-front reverse fault may drag a basin downward and result in large-scale flexural deformation of the lower plate, generating additional accommodation space [*Simpson*, 2014]. Finally, the onset of escape tectonics was proposed to have terminated foreland propagation within the eastern European Alps [*Ortner et al.,* 2015].

On the other hand, the potential impact of foreland basin sediments on orogenic processes has remained largely unnoticed [see, e.g., *Jeanbourquin*, 1994; *Oncken et al.,* 1999; *Remitti et al.,* 2007]. At early stages, peripheral foreland basins are underfilled and characterized by the deposition of platform carbonates, hemipelagic carbonaceous muds and, deep-water turbiditic siliciclastic sediments (i.e., the "underfilled trinity" of *Sinclair* [1997a]). With the progressive underthrusting of the passive margin beneath the upper plate, the sediments are overridden and incorporated into the embryonic orogenic wedge. The setting resembles the one of accretionary wedges, where trench-fill sediments are scraped off from the subducting plate and transferred to the upper plate. Moreover, the mechanical impact of sediments on tectonic processes in

accretionary prisms has become a major research topic in the study of convergent margins (for reviews see *Moore et al.* [2007], *Saffer and Tobin* [2011], and *Ujiie and Kimura* [2014]). From today's perspective, there are two principal outcomes: First, the mechanical properties of sediments change significantly throughout their diagenetic alteration from a porous, unconsolidated soft sediment to a well-compacted rigid rock. As this transformation occurs syntectonically, it affects the way in which deformation is accommodated across the accretionary wedge [e.g., *Morgan and Karig*, 1995; *Kimura et al.,* 2007]. Second, diagenetic dehydration reactions and sediment compaction liberate considerable amounts of fluids, while the porosity and permeability decrease. This configuration results in high pore fluid pressures, which keep the effective stresses in the wedge and along plate boundary fault low, promoting the subduction of the oceanic lithosphere [e.g., *Moore and Vrolijk*, 1992; *Wang*, 1994; *Moore and Saffer*, 2001; *Lamb*, 2006].

These insights from active accretionary margins suggest that the incorporation of unconsolidated foreland basin sediments into an orogenic wedge must be expected to influence initial mountain building processes. Interestingly, *Sinclair* [1997a, 1997b] demonstrated for the example of the European Alps that the underfilled foreland basin and thrust wedge migrated for ~150–200 km in an approximately stable manner over the lower continental plate. This finding is remarkable, considering that the structure of the overridden plate changed over the same distance from an extended rift margin to stable continental crust [*Mohn et al.,* 2014], which might be expected to leave a discernable signature in the basin evolution. Such a signature, however, cannot be inferred [*Sinclair*, 1997b], and the factors that facilitated the "smooth advance" of the orogenic wedge remained unknown. In this respect, we revisit the tectonic evolution of the north central European Alps, focusing on the Glarus Alps in eastern Switzerland. The area provides excellent insights into the prograde evolution of a collisional orogen, ranging from the closure of the oceanic basin, to the inversion of a foreland basin, and the emplacement of nappes along orogen-scale out-of-sequence thrusts. We present a structural analysis integrating observations from the microscale, mesoscale, and macroscale and discuss our results in the context of diagenetic processes and observations from modern accretionary systems.

2. Geological Context

2.1. Tectonic Setting of the Study Area

The European Alps are a collisional orogen resulting from the closure of the Alpine Tethys and the subsequent collision of the European and Adriatic plates [*Dewey and Bird*, 1970; *Frisch*, 1979]. The subduction of the Alpine Tethys, comprising the South Penninic ocean, the Briançonnais continental swell (Middle Penninic), and the North Penninic Valais trough beneath the Adriatic plate, commenced in the Cretaceous [e.g., *Schmid et al.,* 2004; *Handy et al.,* 2010]. The trailing edge of the passive European margin entered the subduction zone during the Eocene. The subsequent partial subduction of the European continental crust and the increasing collision with the Adriatic plate resulted in the formation of a complex orogenic belt.

The Glarus Alps in eastern Switzerland expose four major tectonic elements that provide detailed insights into the tectonic evolution of the orogenic front since the initial subduction of the continental margin (Figure 1): (1) remnants of the Penninic accretionary wedge comprising sediments of the Valais trough, (2) the accreted sediments of the underfilled North Alpine Foreland Basin (in the following simplified referred to as "flysch"), (3) the Helvetic nappes, and (4) an external crystalline massif, the Aar massif. The Penninic accretionary wedge developed at the orogenic front during the subduction of the Valais trough. With the closure of the trough during the early to middle Eocene, the North Alpine Foreland Basin (NAFB) initiated, which is recorded by the sedimentation of the first orogenically derived flysch sediments in the Ultrahelvetic realm, i.e., the southernmost part of the passive European margin. Sedimentation of the Ultrahelvetic flysch terminated ~40 Ma indicating that the European margin entered the subduction zone [e.g., *Sinclair and Allen*, 1992; *Lihou*, 1996]. Simultaneously, the depocenter of the NAFB migrated northward, as recorded in the successive deposition of the Southhelvetic and Northhelvetic flysch units between ~43 and ~34 Ma. [e.g., *Pfiffner*, 1986; *Sinclair and Allen*, 1992]. Throughout the partial subduction of the European margin, the three flysch units (Ultrahelvetic, Southhelvetic, and Northhelvetic) were not underthrusted but scraped off from their substratum and accreted in sequence to the Penninic accretionary wedge [*Lihou*, 1996]. This imbricated nappe stack is called Infrahelvetic flysch units (IFUs, see below). The suture between the Penninic wedge and the accreted flysch units, the so-called Penninic basal thrust, remained active as out-of-sequence thrust (OOS-thrust), resulting in the burial of the accreted flysch units [*Pfiffner*, 1986; *Lihou*, 1996].

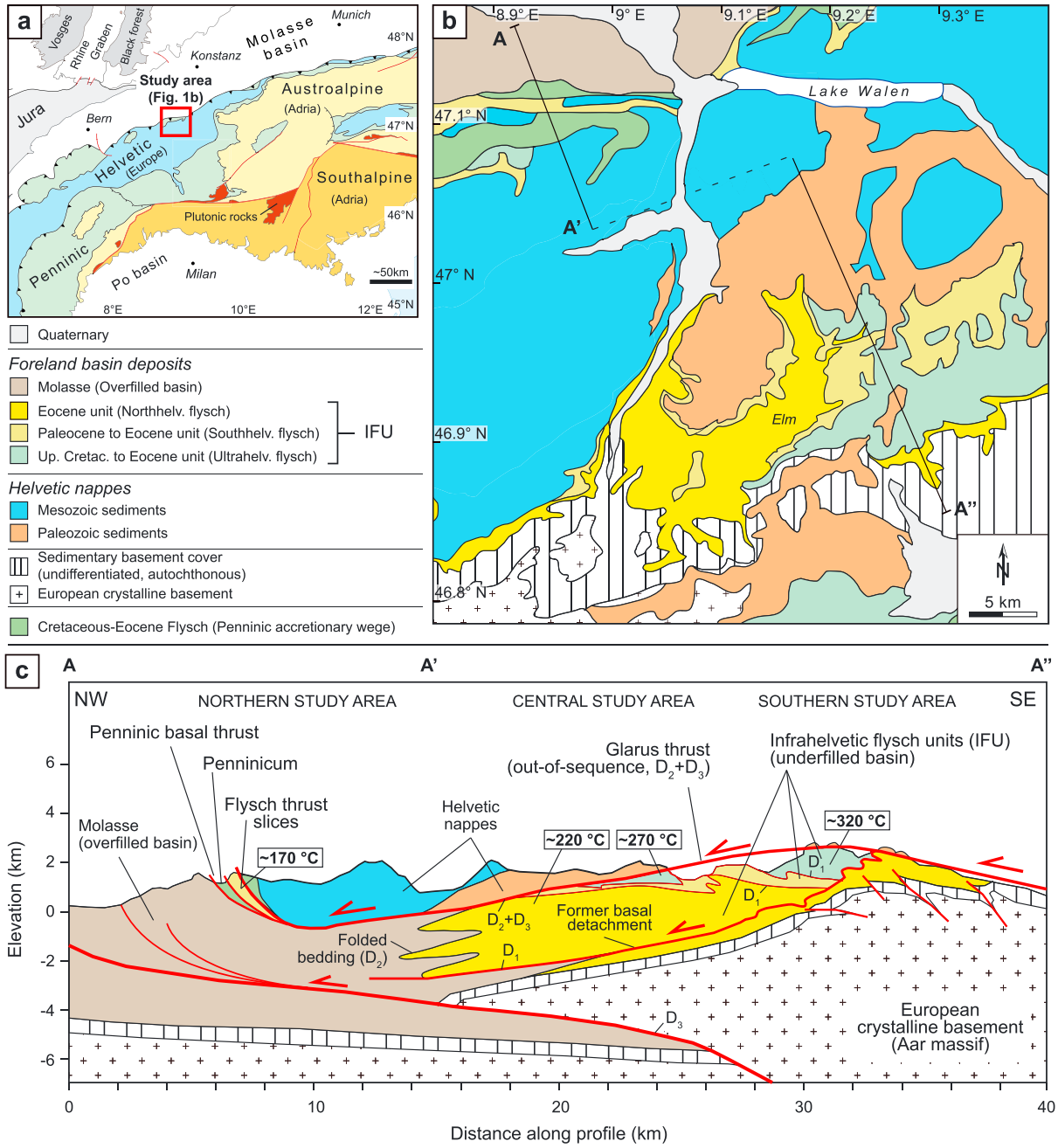

Figure 1. Geological overview. (a) Tectonic sketch of the central and western European Alps showing the location of the study area (based on *Schmid et al.*, [2004]). (b) Geological map of the study area. The line A-A′-A″ locates the cross section shown in Figure 1c. (c) Synthetic and simplified cross section through the study area. The cross section approximately correlates with the transect examined in the present study. Geological map in Figure 1b and cross section in Figure 1c modified from *Pfiffner* [2011].

The Helvetic nappes represent the Paleozoic to Mesozoic preorogenic sedimentary cover of the southern European margin and comprise thick sequences of Jurassic to Cretaceous shelf and slope sediments plus minor amounts of Permian to Triassic sediments [e.g., *Trümpy*, 1969]. In contrast to the flysch units, the Helvetic nappes were not frontally accreted but underthrusted and subsequently underplated by duplex accretion to the base of the Alpine wedge. Underplating probably coincided with metamorphism, which reached greenschist facies conditions in the south Helvetic nappes around 35–30 Ma [*Hunziker et al.*, 1986]. In the following, the Helvetic nappes were thrusted toward the foreland along huge out-of-sequence-thrusts (e.g., the Glarus thrust) that cut through the IFUs. Burial under the advancing Helvetic nappe stack caused

peak metamorphism in the flysch units around 25–20 Ma, reaching subgreenschist facies conditions in the southernmost parts [*Frey et al.*, 1980; *Hunziker et al.*, 1986; *Rahn et al.,* 1995; *Lahfid et al.,* 2010]. The prograde evolution of the orogenic wedge culminated around this time. Simultaneously, deformation relocated into the European continental crust resulting in the underplating of the Aar massif [e.g., *Burkhard*, 1990; *Kempf and Pfiffner*, 2004]. The retrograde evolution and exhumation of the orogenic wedge [e.g., *Glotzbach et al.,* 2010] is not further considered here.

2.2. Structural Evolution of the Infrahelvetic Flysch Units

The structural evolution of the IFUs was thoroughly studied and is classically divided into three major deformational phases [*Schmid*, 1975; *Milnes and Pfiffner*, 1977; *Pfiffner*, 1986; *Lihou*, 1996; *Ring et al.,* 2001]. The first phase (D_1) covers the imbrication of the IFUs. Except for the imbricate thrust faults, i.e., the tectonic contacts between the flysch units, no deformation structures in the IFUs were attributed to this phase. Deformation associated with the D_1 phase has therefore remained enigmatic. The second phase (D_2) is considered as the main Alpine deformation event that took place under (peak) metamorphic conditions and includes (1) folding of the stacked IFUs into NW vergent isoclinal folds, (2) formation of a SE dipping tectonic axial planar cleavage, and (3) OOS-thrusting of the Helvetic nappes along the Glarus fault (Figure 1). The different deformation events were brought into a casual relationship, in which folding and cleavage formation result from the emplacement of the Helvetic nappes [e.g., *Milnes and Pfiffner*, 1977; *Lihou*, 1996]. The observation that the Glarus thrust cuts through already folded flysch units, however, suggested some diachrony in the evolution [*Pfiffner*, 1986]. Additionally, *Gasser and den Brok* [2008] documented hectometer sized folds that formed before cleavage formation and out-of-sequence thrusting and introduced further local deformation phases. Similar, OOS-thrusting within the IFUs is not restricted to activity of the Glarus thrust but was active before. This is evident by the emplacement of tectonic mélanges (Wildflysch nappes) and slices of Helvetic limestones (Subhelvetic units) on top of the IFU before the whole nappe stack was cut by the Glarus thrust [*Trümpy*, 1969; *Lihou*, 1996; *Gasser and den Brok*, 2008]. The occurrence of isolated thrust slices of Northhelvetic and Southhelvetic flysch in the northernmost part of the study area further indicates early stages of OOS-thrusting (Figure 1). These units never experienced temperatures above 160–180°C and must had been transported to the north, before metamorphism in the IFUs occurred [e.g., *Rahn et al.,* 1995]. The third deformation phase (D_3) refers to thrusting along the Glarus fault that followed the D_2 thrusting event. The differentiation is made because the D_3 thrusting event offset metamorphic isograde along the fault plane, indicating that it took place after peak metamorphism [*Frey*, 1988]. During this late stage of thrusting, a crenulation cleavage developed in the direct footwall of the thrust [*Schmid*, 1975; *Milnes and Pfiffner*, 1977]. The timing of the D_3 deformation event is poorly constrained. However, apatite fission track data from the IFUs suggest that the Glarus fault originated as simple landward dipping thrust fault and achieved its present arcuate geometry during exhumation of the wedge after ~10 Ma [*Rahn et al.,* 1997; *Rahn and Grasemann*, 1999]. Some of the postmetamorphic thrusting occurred probably during this time [*Ebert et al.,* 2007].

3. New Insights into the Deformation of the Infrahelvetic Flysch Units

In the following we present new structural observations from the IFUs. All data were collected along a ~30 km long N-S running transect that exposes all three flysch units (Figure 1c). Peak metamorphic temperatures vary between 160–180°C in the north and 300–320°C in the south. The degree of deformation increases toward the south and differs between the flysch units, where the structurally highest unit (Ultrahelvetic) shows the strongest deformation and the structurally lowest unit (Northhelvetic) the weakest. Beside this overall trend, deformation is heterogeneously distributed, varies with rock type (i.e., clay, marl, lime, silt, and sandstones) and may range on the outcrop scale from weak to strong. For clarity, we present our observations in a summarized form and give detailed information on locality, lithology, temperature, etc. only where necessary.

3.1. Structures in Weakly Deformed Rocks

Different kinds of deformation structures were only found in weakly deformed rocks and are described in the following. They are generally nonpenetrative and spatially very restricted. The structures often represent the only recognizable overprint of the primary sedimentary fabric and comprise sediment injections, deformation bands, microfaults, centimeter-scaled folds, and structurally bounded pressure solution seams. Sediment injections occur within turbiditic sequences and are up to ~60 cm thick (Figures 2a–2c). Usually, coarse sands are injected from the base of turbidites into the overlying silty and clayey layers, but the

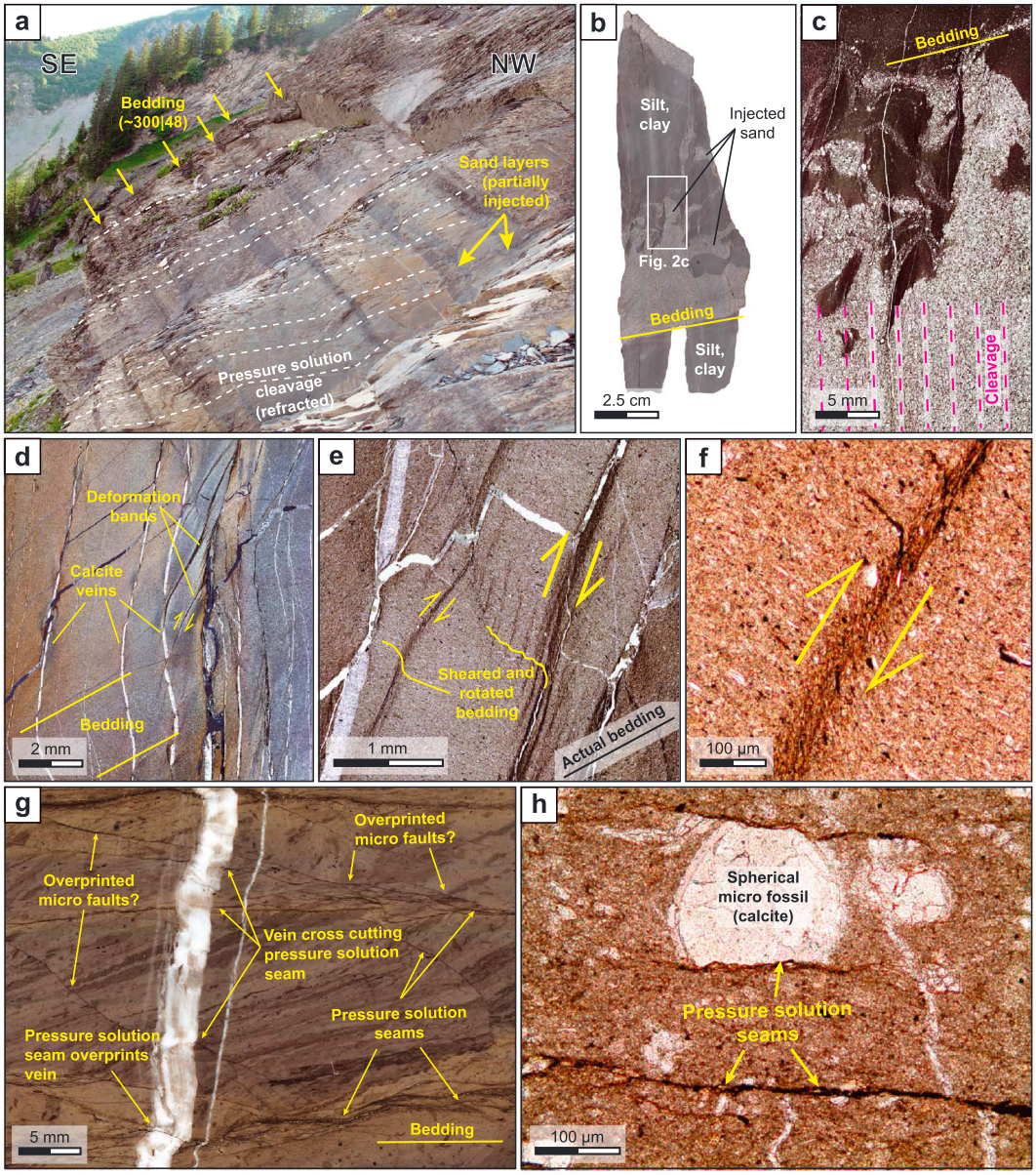

Figure 2. Deformation structures in weakly deformed rocks. (a) Turbidites in the Northhelvetic flysch (46.9363°N, 9.1554°E). The photo shows the upper limb of an anticline, the bedding dips with ~50° toward the NW. Sands are partially injected from the base of the turbidites into the overlying clay-rich layers. The sediment injections are interpreted to reflect deformation within a basinal setting in front of the advancing orogenic wedge. The dashed line indicates the trace of the pressure solution cleavage (refracted), which formed at a later stage of the structural evolution. (b) Example of sediment injection in a hand specimen sampled in the outcrop shown in Figure 2a. The sample is rotated ~50° counterclockwise relative to its orientation in the field. (c) Microphotograph of the injection structure shown in Figure 2b. The sediment injection is weakly overprinted by a pressure solution cleavage formed at a high angle to bedding. (d–f) Examples of deformation bands (46.9961°N, 9.0881°E). The bedding is rotated and sheared near the deformation bands resulting in a local reorientation of the bedding planes. The deformation bands overprint small-scale calcite veins, suggesting a mixed brittle-ductile behavior of the sediments during the formation of these structures (Figure 2e). (g and h) Examples of locally restricted pressure solution. The discontinuities in Figure 2g are interpreted as microfaults or shear surfaces. Pressure solution is restricted to these anisotropies and does not occur in the adjacent host rock. Pressure solution is also common along interfaces between sediment and microfossils (Figure 2h) (47.1934°N, 9.2317°E). See text for details.

injection of clays into coarse sandstones was also documented. Deformation bands are millimeter to centimeter sized, planar, or slightly anastomosing kink-like shear zones that are preserved within clayey to silty sediments (Figures 2d–2f). They developed at a high angle to bedding (~60–80°) and show a reverse sense of shearing. In some cases the deformation bands overprint small-scale extension veins and offset them by less then 1 mm (Figure 2d). Macroscopically, these features cannot be identified in the field or in hand specimens. Microscopically, deformation bands can be recognized by the deflection and kinking of the bedding-parallel rock fabric, like aligned sheet silicates. In some cases, we observed ductile shearing within a wider zone around the deformation band associated with a rotation of bedding by several degrees. The bands appear in plane-polarized light darker than the host rock (Figures 2e and 2f). As there is no change in the mineralogy within the deformation bands, the darker appearance may result from a reduction in porosity related to the formation of the bands.

Microfaults are supposed to form a network of anastomosing shear surfaces which we observed near the base of an isolated thrust slice of Southhelvetic flysch cropping out in the northern study area (Figures 1c and 2g). The microfaults are developed on the millimeter to centimeter scale. The supposed shear structures, however, are ambiguous as we can neither identify a clear shear sense nor striations, due to an overprint of the supposed surfaces by pressure solution. Alternatively, these structures may originate from pressure solution solely, although their distinct geometry is difficult to explain then. Anyhow, pressure solution in weakly deformed rocks is often linked to preexisting structures, spatially very restricted, and limited to the dissolution of carbonates. For example, pressure solutions seams are commonly found along sediment-fossil interfaces, but they rapidly die out away from the fossil, although isolated seams without a visible structural relationship may also occur (Figure 2h). Such pressure solution seams are sometimes crosscut by calcite veins, while the same veins are in turn overprinted by pressure solution. This mutually crosscutting relationship suggests that the site of active dissolution changed throughout the development of the rock fabric. Pressure solution can also be contemporaneously active with other deformation mechanisms, like brittle fracturing and particulate flow, i.e., frictional grain boundary sliding with no or only little breaking of single sediment particles [e.g., *Borradaile*, 1981; *Maltman*, 1994]. This is documented by the shortening and folding of bedding-parallel calcite shear veins in the central part of the study area (G_1 veins, see below; Figures 3a–3d). The veins are embedded in a fine-grained sediment matrix that exhibit a microbedding of alternating silt and marl layers (Figure 3b). After vein formation, the sediments experienced bedding-parallel contraction. In the vein, shortening is primarily accommodated by brittle fracturing and rotation of the fragments, while the surrounding sediments are deformed in a rather ductile manner, i.e., in a continuous way without recognizable discrete fractures. In the marly layers shortening is accompanied by pressure solution of carbonates, while it is largely assisted by particulate flow within the silty layer. This contrasting mechanical behavior is depicted in the changing thickness of the deformed layers. Due to the dissolution of carbonates, the thickness of the marl is reduced by $>$90 vol % in the limbs and hinges. In contrast, the silt layers show no significant thickness changes across the fold (Figures 3b and 3c).

3.2. Folding and Stratal Disruption

Folding in the IFUs was described by several authors and is summarized in section 2.2. In addition to the previous descriptions, we like to highlight two further aspects. First, in contrast to regional-scale folds that affect the whole imbricated nappe stack of the IFUs and are thought to be associated with a axial planar cleavage, we documented folds that record a similar shortening direction (approximately NW-SE) but exhibit no axial planar cleavage [see also *Gasser and den Brok*, 2008]. For example, bedding planes in the hanging wall of imbricate thrust faults are disharmonically folded, but the folds exhibit no tectonic cleavage (Figures 4a and 4b; see below). Likewise, fault-propagation folds developed on the decameter scale within shales and siltstones of the Northhelvetic flysch exhibit no tectonic cleavage (Figure 4c).

The second aspect concerns the occurrence of stratal disruption within the limbs of folds. Stratal disruption refers to the shearing, extension, and dismemberment of competent beds that were originally intercalated in less competent strata [e.g., *Festa et al.,* 2010]. In the IFUs, stratal disruption occurs basically in shales with intercalated arenaceous turbidites and is common in the Southhelvetic and Ultrahelvetic units (Figure 4d). The degree of disruption ranges from almost zero (i.e., the original bedding is largely preserved) to very intense disruption, in which case isolated sandstone blocks float in a shaly matrix (Figure 4e). In most cases, disrupted sandstone layers show a pinch-and-swell or boudin-like geometry (Figures 4d and 4e). The shape

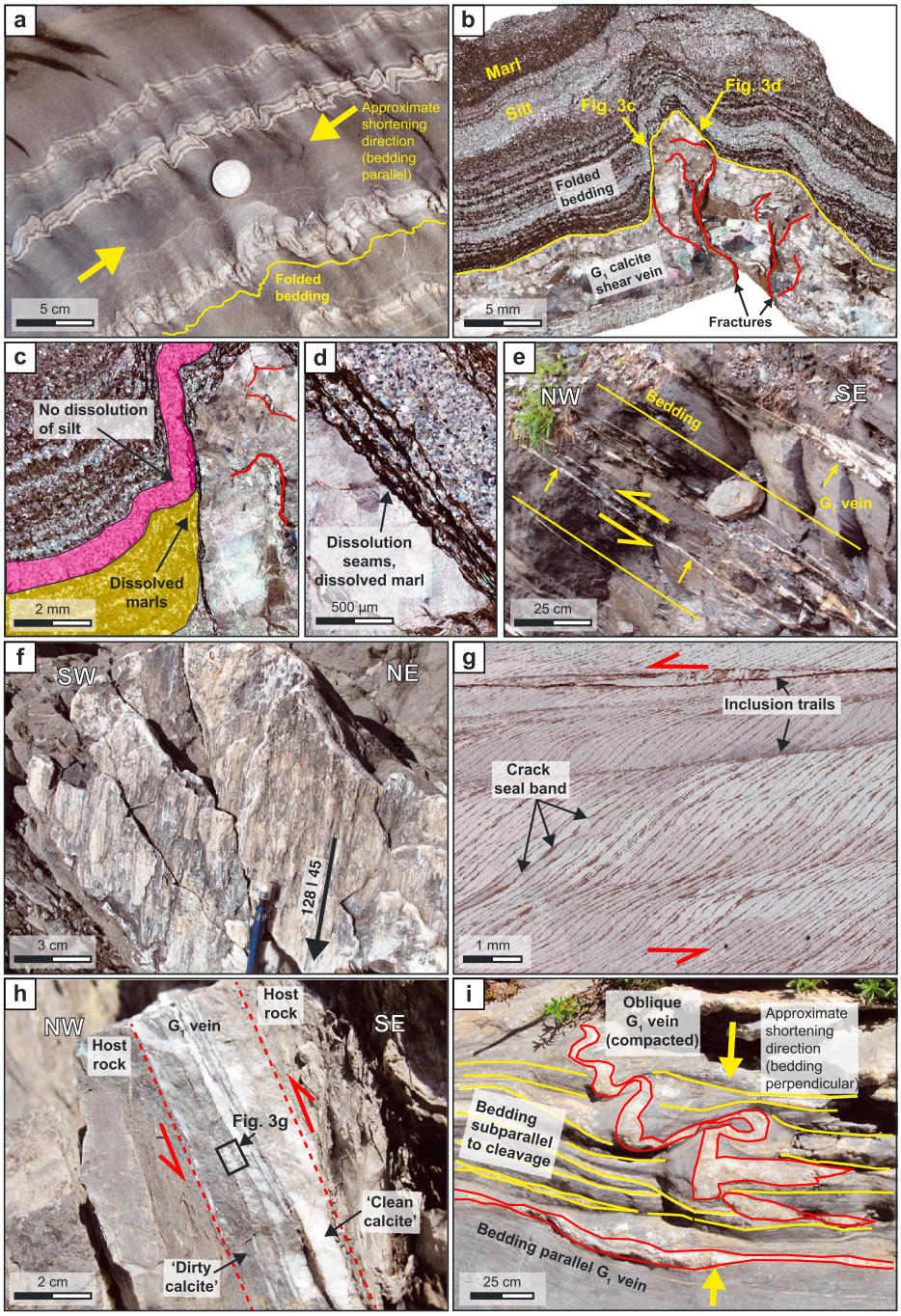

Figure 3. Sediment deformation and G_1 calcite shear veins. (a) Folded bedding indicating bedding-parallel shortening (46.9961°N, 9.0881°E). (b) Bedding-parallel calcite shear vein that was folded together with bedding. Sample from Figure 3 a. Shortening of the calcite vein was largely accommodated by brittle fracturing (red lines) and rotation of the fragments. In contrast, the silt and marl layers were shortened in a ductile manner, i.e., by particulate flow and pressure solution of carbonate particles, respectively. (c and d) Details of Figure 3b. (e) Examples of bedding-parallel calcite shear veins (G_1 veins) (46.9096°N, 9.1911°E). Shear sense is top-to-the-NW. (f) Top view on the surface of a G_1 vein showing a clear lineation. The lineation is parallel to the transport direction. (g) Microphotograph showing the typical microstructure of G_1 veins. The long axis of the picture is parallel to lineation of the vein. The inclusion trails and crack-seal bands consist of host rock particles and indicate a top-to-the-NW shear sense. See text for detail. (h) Example of G_1 vein containing clay particles and host rock fragments. The inclusions give the calcite a dirty appearance, almost similar to the color of the host rock. Shear sense top-to-the-NW. Microstructures in Figure 3g are from the mineral vein shown in Figure 3h. (f–h) All (47.1407°N, 9.1073°E). (i) Example of a G_1 vein that formed at an oblique angle to bedding (46.9816°N, 9.1878°E). The oblique vein was shortened and folded during sediment compaction and subsequent tectonic deformation (note the boudinage of the structures).

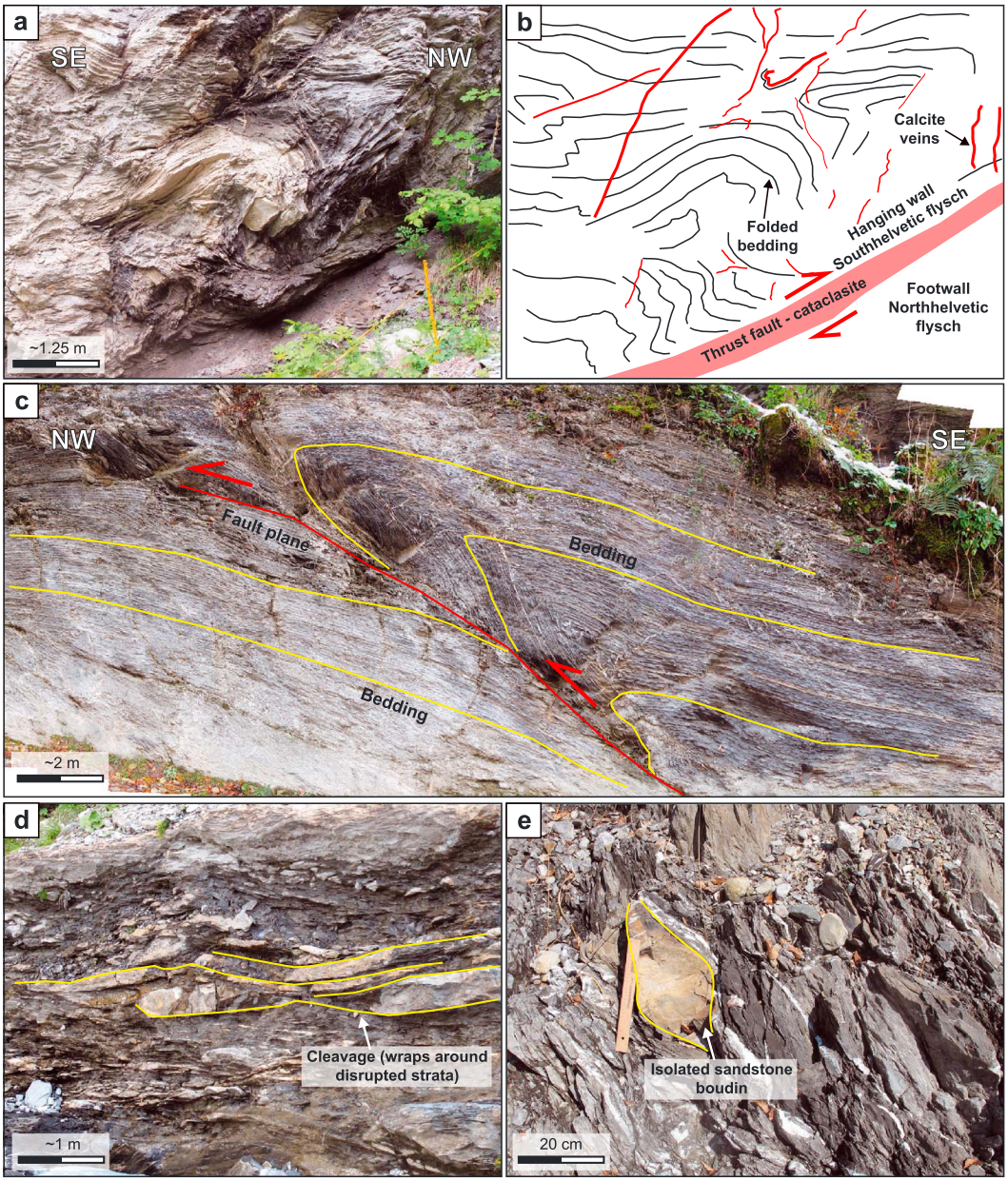

Figure 4. Folding and stratal disruption. (a and b) Tectonic contact between the Southhelvetic flysch (hanging wall) and Northhelvetic flysch (footwall) (46.9891°N, 9.1573°E). Bedding in the hanging wall is folded. The folds are neither associated with the formation of an axial planar cleavage nor with pressure solution. The thrust plane is defined by a cataclasite. (b) Interpretation of Figure 4a. (c) Fault-propagation fold. Similar to the folds in Figure 4a the fault-propagation fold is not associated with an axial planar cleavage or pressure solution (46.9889°N, 9.1558°E). (d and e) Examples of stratal disruption. The pressure solution cleavage in Figure 4d is subparallel to bedding and wraps around the disrupted sandstone strata, suggesting that cleavage formation was syntectonic to posttectonic to stratal disruption (46.9023°N, 9.1867°E). (e) Isolated sandstone boudin floating in a clay-rich matrix (47.1407°N, 9.1073°E).

of boudins is rather drawn than blocky suggesting ductile deformation during stratal disruption, most probably related to particulate flow. However, mineral veins in sandstone boudins indicate also phases of brittle rock failure (Figure 4e), suggesting an overall mixed brittle-ductile rheology during stratal disruption. We observed stratal disruption in areas in which the tectonic cleavage is oriented subparallel to bedding, suggesting a position within a fold limb (Figure 4d). This finding concurs with observations by *Lihou* [1996], who documented the boudinage of a thick limestone unit (Nummulitic formation, Southhelvetic flysch) also within the limbs of hectometer-scaled folds.

3.3. Foliations and Cleavage Formation

The foliation in the IFUs is heterogeneously developed and can be differenced into a primary diagenetic foliation (or bedding plane fissility) and a secondary tectonic pressure solution cleavage. The diagenetic foliation is preserved within the northern and central part of the study area and defined by the orientation of platy minerals (e.g., micas) subparallel to bedding (Figure 5a). The foliation is not linked to pressure solution or the growth of new micas. It is considered to result from the orientation of platy minerals subparallel to bedding during sedimentation and subsequent sediment compaction [e.g., *Passchier and Trouw*, 2005]. In the central and southern parts of the study area, especially in the Southhelvetic and Ultrahelvetic units, the diagenetic foliation is overprinted by the pressure solution cleavage. The cleavage is defined by the dissolution of quartz and calcite grains and the accumulation of the insoluble phases (e.g., micas, iron oxides, and organic material) as pressure solution seams (Figures 5b and 5c). In contrast to the isolated and nonpenetrative pressure solution seams that occur in the northernmost part of the study area (section 3.1), the pressure solution cleavage is penetrative, i.e., it forms a laterally continuous foliation plane. The characteristic of the cleavage, however, varies with rock type. It is well expressed in argillaceous rocks but only weakly developed in sandstones. In fold limbs the pressure solution cleavage is oriented subparallel to the diagenetic foliation and overprints it. The transition between both structures is generally smooth, which makes it sometimes difficult to distinguish them. In contrast, the pressure solution cleavage makes a high angle to bedding in fold hinges and is well distinguishable from the diagenetic foliation (Figure 3c).

3.4. Mineral Veins

Mineral veins are a ubiquitous feature in the IFUs and can be prograde or retrograde. *Dielforder et al.* [2015] described three groups of mineral veins (G_1, G_2, and G_3 veins) that developed during the prograde evolution and occur independently from other tectonic structures. G_1 veins comprise bedding-parallel calcite shear veins (Figure 3e). The veins have a lineation and show an internal layering and a segmentation, which are defined by inclusion trails and crack-seal bands, respectively (Figures 3f and 3g). Both the lineation and the crack seal bands indicate a top-to-the-NW shear sense (for details on vein microstructures see *Labaume et al.* [1991] and *Koehn and Passchier* [2000]). Disperse inclusions of fine host rock fragments and clay minerals can give the vein carbonate a dull appearance and suggests a formation of the veins in poorly consolidated sediments (Figures 3g and 3h) [cf. *Labaume et al.,* 1991]. This interpretation is in good accordance with the strontium and oxygen isotope systematics of vein carbonates indicating that G_1 veins formed under early diagenetic conditions (~40–70°C) (for details see *Dielforder et al.* [2015]). Sometimes, a conjugate set of G_1 veins is developed at an oblique angle to bedding (Figure 3i). The oblique veins are folded and record bedding perpendicular shortening of ~30–60%. Bedding and G_1 veins can be slightly boudinaged and are overprinted by a pressure solution cleavage subparallel to bedding. We interpret the overall rock fabric to result from the diagenetic compaction of the sediment during or after the formation of G_1 veins as well as from subsequent phases of tectonic compaction associated with layer parallel extension (see also sections 3.3 and 5.1).

G_2 and G_3 veins comprise quartz-calcite veins that record phases of extensional rock failure within the wedge (see *Dielforder et al.* [2015] for details). G_2 veins represent mineralized fault cores of south dipping normal faults and contain centimeter-sized brecciated host rock fragments (Figure 5d). G_3 veins form steep, north dipping extension fractures that formed parallel to the orientation of the largest principal stress (Figure 5e). In contrast to G_1 veins, the quartz and calcite crystals in G_2 and G_3 veins are devoid of fine-grained host rock inclusions. Oxygen isotope thermometry suggests that the veins formed during later stages of the prograde evolution at temperatures of ~200–300°C (for details see *Dielforder et al.* [2015]). At first sight, G_2 and G_3 veins crosscut the pressure solution cleavage (Figures 5e and 5f). Detailed crosscutting relationships, however, indicate that the veins were affected by continuous pressure solution and associated with layer perpendicular shortening in the IFUs. For example, G_3 veins are sometimes folded into open folds with long wavelengths and low amplitudes (Figure 5e). Moreover, stylolithic pressure solutions seams comprising iron hydroxides occur within the veins, suggesting that shortening during folding was accommodated by vein-internal pressure solution (Figure 5g).

Besides the G_1, G_2, and G_3 veins described above, we observed additional kinds of mineral veins in the study area that are difficult to group. Some of these veins can be related to folding and thrust faulting and

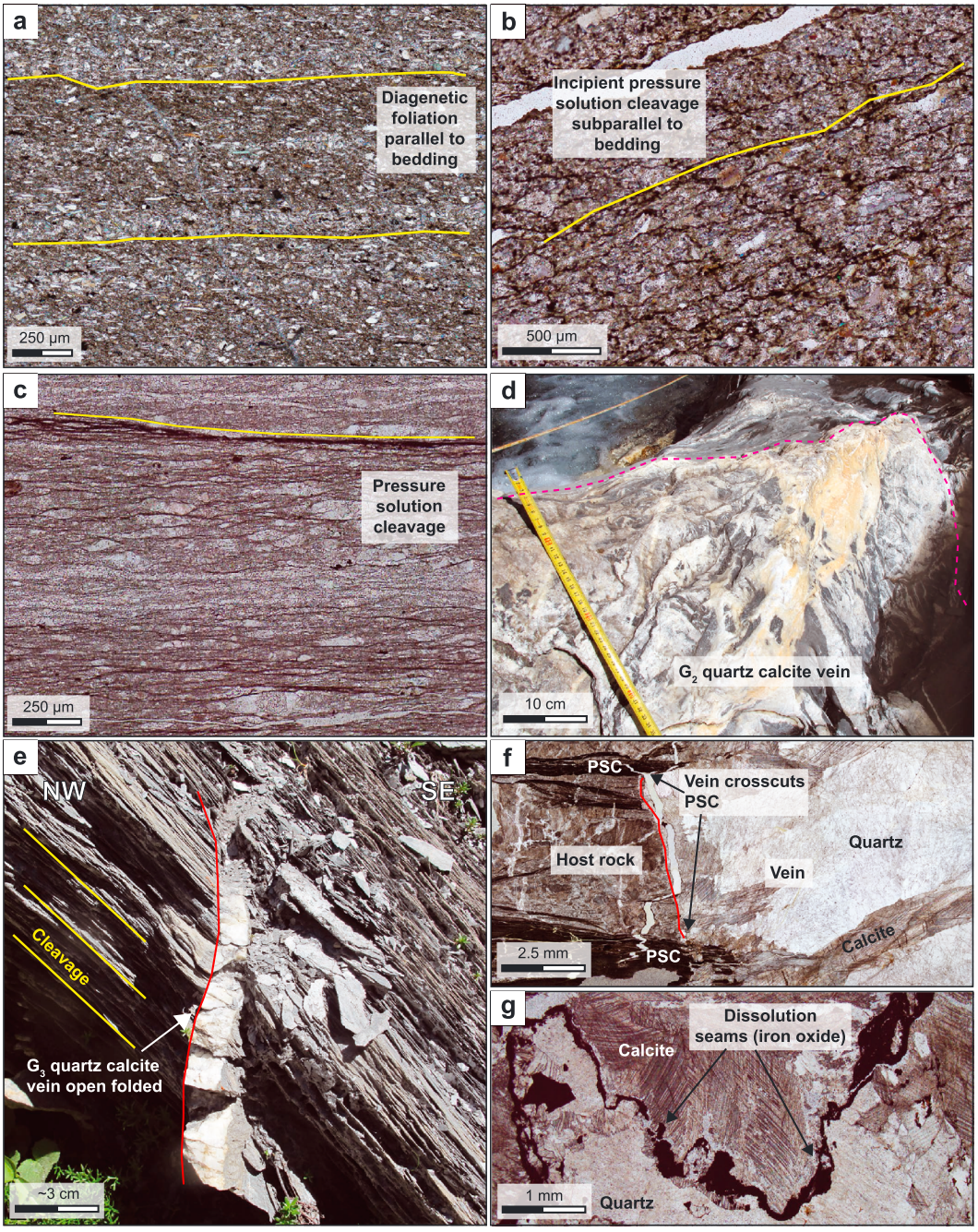

Figure 5. Cleavage development and quartz-calcite veins. (a) Diagenetic foliation parallel to bedding; siltstone (46.9961°N, 9.0881°E). (b) Incipient pressure solution cleavage subparallel to bedding; fine-grained sandstone (46.9118°N, 9.1893°E). (c) Pressure solution cleavage in marlstone. (d) G_2 quartz-calcite vein. G_2 veins record extensional faulting within the study area and formed at temperatures of ~200–300°C (46.8912°N, 9.1853°E). The vein contains massive fragments of foliated host rock. (e) G_3 quartz calcite vein crosscutting the pressure solution cleavage (46.8923°N, 9.1878°E). The vein is slightly deformed into an open fold due to continuous pressure solution after vein formation. G_3 veins formed over the same temperature range than G_2 veins. (f) Detail of G_3 vein crosscutting pressure solution cleavage (49.9019°N, 9.2245°E). (g) Pressure solution seam comprising iron oxides in G_3 vein (Figure 5e). The seam indicates that pressure solution in the study area continued after the formation of the quartz-calcite veins at temperatures of ~200–300°C.

are discussed in the respective section (i.e., sections 3.2 and 3.5). Moreover, we documented mineral veins that crosscut all other structures and form open clefts with idiomorphic quartz and calcite crystals (Figure 6i). We interpret these veins to be formed on the retrograde path and exclude them from further considerations.

3.5. Thrust Faults

The tectonic contacts between the different flysch units represent former imbricate thrust faults that formed during the accretion of the IFUs. We inspected both contacts, i.e., between the Ultrahelvetic and Southhelvetic flysch and between the Southhelvetic and Northhelvetic flysch. At the contact between the Ultrahelvetic and Southhelvetic flysch, Upper Cretaceous to Paleocene sandstones are thrusted on top of Eocene marlstones (Figure 6a). The bedding is well preserved in both blocks and a brittle overprint of the rock fabric occurs only close to the thrust plane. The actual plane is defined by a cataclasite of a few millimeter to centimeter thickness that comprises material derived from the hanging wall and footwall (Figure 6c). Grain size reduction in the cataclasite is moderate (Figures 6d–6f). Calcite extension veins occur within the lowermost ~10 cm of the hanging wall and have a high angle to the thrust plane. They contain fragments of the cataclasite supporting a formation during imbricate thrusting. We further documented small thrust faults within the uppermost ~10 m of the footwall that are interpreted as splays of the actual imbricate fault (Figure 6b). Similar to the main fault, the bedding is cataclastically reworked along the fault surfaces. The faults show a mutually crosscutting relationship with calcite extension veins that we interpret to be formed during imbricate thrusting. At the contact between the Southhelvetic and Northhelvetic flysch unit, Eocene marls are thrusted on top of younger Eocene siltstones (Figures 4a and 4b). The fault contact is defined by a several centimeter thick cataclasite comprising material from the footwall and hanging wall. The bedding in the hanging wall is folded into noncylindrical, disharmonic, and irregular folds that developed on the meter scale. Extensional calcite veins crosscut the folded strata or are folded together with bedding. Likewise for the other contact, we interpret the veins and folds to be formed during imbricate thrusting.

Another kind of faults that we documented within the Northhelvetic flysch are flysch internal thrust faults (Figures 6g–6i). The faults are several hundred meters long and have displacements of tens of meters. The fault planes dip to the SE, suggesting that the faults formed in response to the general NW-SE directed shortening. In contrast to the imbricate thrust faults, the hanging walls are intensively fractured and exhibit a dense network of extensional veins that comprise quartz, calcite, chlorite, and white mica. We associate these veins with faulting (Figure 6h). They disrupt well-compacted and cemented host rocks, suggesting that the faults developed at a later stage than the imbricate thrust faults described above. We further documented a set of retrograde clefts that developed at a high angle to the veins in the hanging wall and overprint the faulting related fabric (Figure 6i, see also section 3.3).

4. Temperature Constraints and Fluid Sources

To investigate potential effects of diagenesis on the structural evolution of the IFUs, we set up a simple diagenetic model. It approximates the temperature-depth evolution of the southern part of the study area, i.e., where the highest metamorphic conditions were reached. Afterward, clay dehydration, sediment compaction, and fluid release rates are calculated. The model constraints are described in the following.

4.1. Geothermal Gradient

Geothermal gradients that persisted during the prograde evolution of the frontal orogenic wedge are only poorly constrained. Previous estimates of ~30°C km^{-1} are either adoptions of average geothermal gradients inferred for stable continental crust or derived from data that reflect temperature gradients on the retrograde path of the orogen [e.g., *Frey*, 1988; *Pfiffner*, 1986; *Herwegh and Pfiffner*, 2005] and should not be borrowed for considerations on the prograde evolution. We therefore constrain the geothermal gradient by calculating the temperatures along the former plate boundary fault that was active during the accretion of IFUs. As the flysch units remained in a structural position close to the fault, the geothermal gradient in the IFUs is approximately the same than the one calculated for the fault. Our calculations follow the works of *Molnar and England* [1990] and *Tichelaar and Ruff* [1993] that provide analytical solutions to calculate temperatures along major thrust faults. The approach considers the heat flow from the underthrusted block Q_0, radiogenic heat production

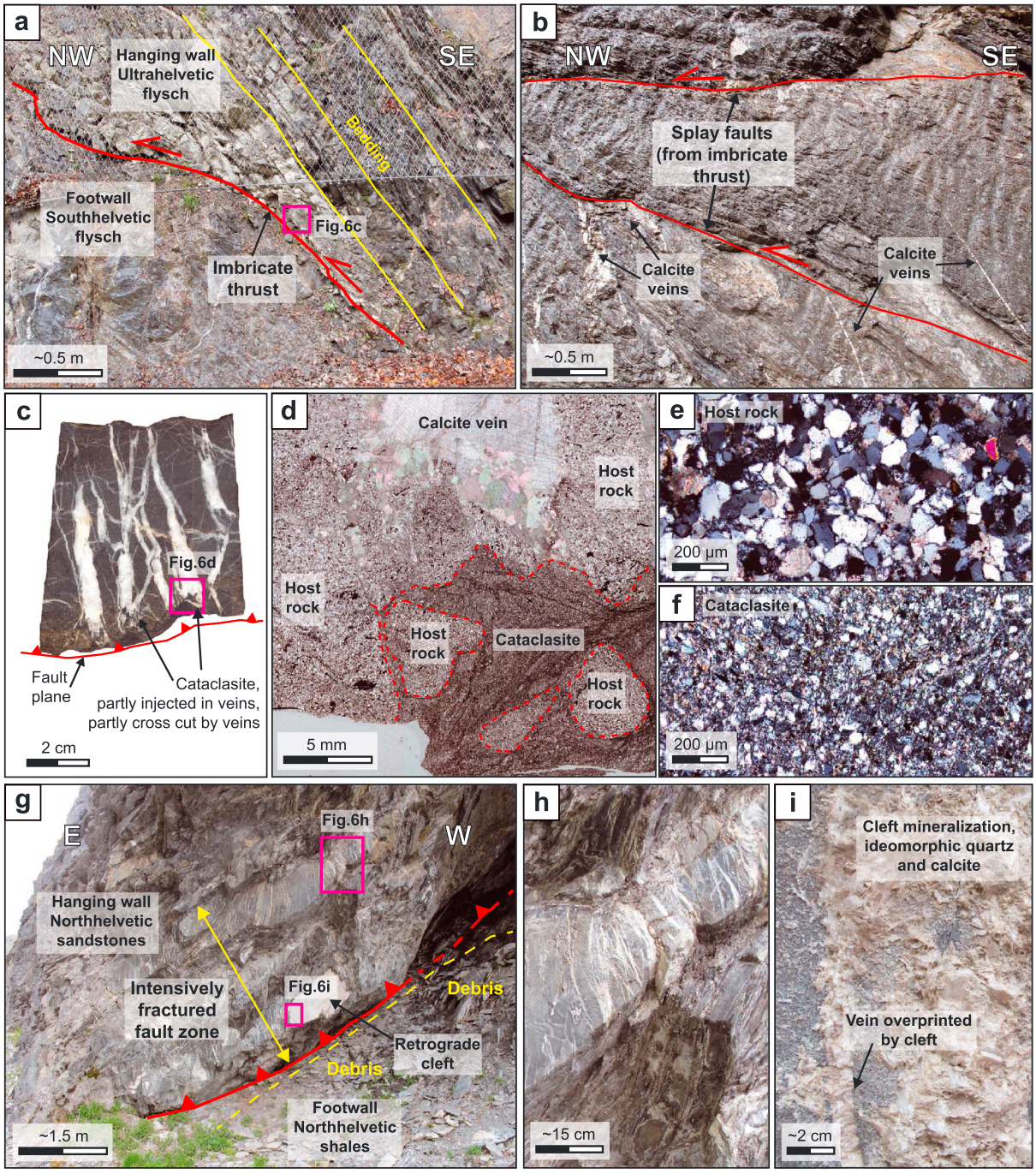

Figure 6. Structural framework of thrust faults. (a) Tectonic contact between the Ultrahelvetic flysch (hanging wall) and Southhelvetic flysch (footwall) (46.9597°N, 9.1881°E). The thrust plane is defined by a cataclasite. (b) Splays in the footwall of the imbricate thrust shown in Figure 6a. The picture was taken ~2 m to the NW of the picture shown in Figure 6a. The splays exhibit a mutually crosscutting relationship with the calcite veins, indicating that vein formation occurred during imbrication. (c) Hand specimen taken in the direct hanging wall of the thrust shown in Figure 6a. The red line indicates the approximate position of the thrust plane. The cataclasite is partly preserved in the lowermost part of the sample. Fragments of the cataclasite occur within the calcite veins suggesting vein formation during imbricate thrusting. (d–f) Thin section micrographs showing details of cataclasite. Crossed nicols. (g) Flysch internal thrust fault (46.8883°N, 9.1273°E). The hanging wall of the thrust is intensively fractured. The abundant mineral veins comprise quartz, calcite, and some minor amounts of chlorite and white mica. (h) Detail of mineral veins within the hanging wall of the thrust shown in Figure 6g. The veins overprint well compacted and cemented rocks. (i) Detail of retrograde cleft mineralization overprinting the fault structure.

Table 1. Model Parameters

Parameter	Description	Value
V (mm yr^{-1})	Plate convergence	2–12
δ (°)	Dip angle of the thrust fault	10
k (W m^{-1} K^{-1})	Thermal conductivity	2.75
k (m^2 s^{-1})	Thermal diffusivity	1×10^{-6}
Q_0 (mW m^{-2})	Surface heat flow of subducting plate	70
ρ (kg m^{-3})	Sediment density	2750
A (μW m^{-3})	Radiogenic heat production	1

in the wedge A, and shear heating τV. All factors are reduced by the divisor S that accounts for the advection of heat due to underthrusting and is given by *Molnar and England* [1990]:

$$S = 1 + b\sqrt{\frac{z_f V \sin(\delta)}{k}} \quad (1)$$

where b is a constant close to 1, z_f is the depth along the fault, V is the convergence rate (see below), δ is the dip angle of the thrust fault (10°) [*Dielforder et al.,* 2015], and k the thermal diffusivity (1×10^{-6} m^2 s^{-1}). All parameters are listed in Table 1. The heat flow from the underthrusted European lithosphere Q_0 is taken to be 70 mW m^{-2}, representing an average value for continental crust [e.g., *Pollack*, 1982; *Davies*, 2013]. The radiogenic heat production A is assumed to be constant with depth and is set to a value of 1 μW m^{-3} [e.g., *Hyndman and Wang*, 1993]. The temperature due to radiogenic heating given by *Tichelaar and Ruff* [1993]

$$T\text{rad} \approx \frac{A z_f^2}{2kS} \quad (2)$$

where k is the thermal conductivity (2.75 W m^{-1} K^{-1}). Shear heating is defined as the product of shear stress τ and convergence rate V. The shear stress on a cohesionless brittle fault is given by Byerlee's friction law:

$$\tau = \mu(1 - \lambda)\rho g z_f \quad (3)$$

where μ is the coefficient of internal friction, λ the pore fluid pressure ratio (i.e., the ratio of pore fluid pressure over lithostatic pressure), ρ the rock density, and g the acceleration due to gravity. In the ductile realm the shear stress on a fault depends on temperature, while temperature depends on shear heating and thus on shear stress. To bypass this interdependency, we follow the approach of *Lamb* [2006] and assume for the calculation of shear heating a constant shear stress of 20 MPa in the upper 25 km of the wedge. The temperature along the plate boundary fault T_f is then given by [e.g., *Lamb*, 2006]:

$$T_f \approx \frac{(Q_o + \tau V) z_f}{kS} + \frac{A z_f^2}{2kS} \quad (4)$$

Reconstructions of the convergence rates during the prograde evolution of the wedge suggest a slowdown from relatively high rates of ~6–12 mm yr^{-1} between ~65 and 30 Ma to relatively low rates of only 2–3 mm yr^{-1} after ~30 Ma [*Pfiffner*, 1986; *Sinclair and Allen*, 1992; *Sinclair*, 1997a]. Solving equation (4) for the highest and lowest convergence rates yields geothermal gradients ~15°C km^{-1} and ~20°C km^{-1} for the upper 25 km of the wedge, respectively. For the mean convergence rate of 7 mm yr^{-1} we obtain a geothermal gradient of ~17°C km^{-1}. We note that the calculated gradients agree well with independent constraints. For example, *Wiederkehr et al.* [2011] report peak metamorphic conditions for metasediments from the distal European margin of ~6–7 kbar and ~350–425°C. In contrast to the IFUs, these sediments were subducted together with the distal European margin and not frontally accreted. Assuming an average density of 2750 kg m^{-3} for the overlying wedge, the peak metamorphic conditions translate to a geothermal gradient of ~16°C km^{-1}, similar to the one we calculated for the average convergence rate. Moreover, *Rahn and Grasemann* [1999] estimated from thermal modeling of apatite fission tracks a geothermal gradient of ~17°C km^{-1} during the late stage exhumation of the IFUs around 10 Ma. Given the good accordance between the independent constraints, we base our following considerations on a geothermal gradient of 17°C km^{-1}.

4.2. Fluid Sources by Sediment Compaction and Clay Dehydration

We calculate the compaction-derived fluid source from presumed porosity changes in the accreted sediments passing through a steady state porosity field [e.g., *Saffer,* 2003; *Lauer and Saffer*, 2015]. The calculations are exemplary for a point within the Northhelvetic flysch. The reference frame is therefore set to the deformation front in the North Alpine Foreland Basin at the time of sedimentation of the basal units of the Northhelvetic flysch, i.e., ~40 Ma [*Sinclair*, 1997a]. The burial rate of the sediments v_b is approximated by assuming a linear burial between the time of sedimentation and the time of peak metamorphism at

~25–20 Ma [*Hunziker et al.,* 1986]. Assuming a geothermal gradient of 17°C km^{-1} and a peak metamorphic temperature of ~320°C [*Lahfid et al.,* 2010], v_b ranges between ~0.9 and 1.3 km Myr^{-1}. The fluid source term for compacting sediments Γ_{com} (V_{fluid}/V_{sed} Myr^{-1}) is given by [e.g., *Saffer*, 2003]

$$\Gamma_{com} = \frac{\partial \phi}{\partial z} v_b \tag{5}$$

where ϕ is the porosity and z the depth within the accretionary complex. The porosity is defined by using a porosity-depth relationship based on the compaction trend summarized by *Bray and Karig* [1985]. The trend was fitted using an exponential function and an initial porosity ϕ_i of 0.6 and a minimum porosity ϕ_{min} of 0.01

$$\phi(z) = (\phi_i - \phi_{min}) exp(-dz) + \phi_{min} \tag{6}$$

where d is a fitting parameter.

Beside sediment compaction, the smectite-illite transformation (S-I) is the largest fluid source during the diagenetic and metamorphic alteration of accretionary prism sediments [e.g., *Moore and Vrolijk*, 1992]. We compute the depth of the S-I transformation along the burial path described above using the kinetic expression of *Pytte and Reynolds* [1988]:

$$\frac{\partial S_{IS}}{\partial t} A_{IS} \exp\left(\frac{-E}{RT}\right) \left(\frac{K^+}{Na^+}\right) {S_{IS}}^5 \tag{7}$$

where A_{IS} is a scaling factor (5.2×10^{-7} s^{-1}), E is the activation energy (1.38×10^{-5} J mol^{-1}), R is the ideal gas constant (8.314 J mol^{-1} K^{-1}), T is the temperature (K), and S_{IS} is the mole fraction of smectite in mixed layer I-S. We assume a conservative initial mole fraction of smectite of $S_{IS,initial} = 0.8$. The ratio [K^+]/[Na^+] is assumed to be in equilibrium with K-feldspar and to be a function of temperature [*Pytte and Reynolds*, 1988]:

$$\left(\frac{K^+}{Na^+}\right) = 74.2 \exp\left(\frac{-2490}{T}\right) \tag{8}$$

The fluid source term from the smectite-illite transformation Γ_{clay} is then calculated for the burial path following *Saffer* [2003]:

$$\Gamma_{clay} = \frac{\partial S_{IS}}{\partial t} HC(1 - \phi) \tag{9}$$

where H is the volumetric water content of smectite (0.4) [*Colten-Bradley*, 1987], C is the volume fraction of the sediment composed of I-S mixed layer clay. X-ray diffraction (XRD) data of ten rock samples from the study area suggest that C is ~0.4–0.6 in clay-rich lithologies and ~0.1–0.3 in carbonaceous marls and siltstones (Table S1 in the supporting information). As we cannot quantify the absolute fractions of clay-rich and clay-poor sediments in the whole accretionary complex, we assume a conservative value of $C = 0.3$.

5. Discussion

The structural evolution of the IFUs was previously described by a deformation scheme that distinguishes the early imbrication of the flysch units (D_1 phase), from ductile and penetrative "Alpine deformation" under metamorphic conditions (D_2 phase) and postmetamorphic deformation on the retrograde path (D_3 phase). Many of our observations agree with this scheme and relate to the first two deformation phases, i.e., to the prograde evolution of the IFUs. In addition, our data set details a sequence of deformation that reflects the changing mechanical behavior of the sediments throughout diagenesis and low-grade metamorphism. In the following discussion, we focus on the latter aspect. To do so, we first identify the relative timing and tectonic setting of the different deformation events. Afterward, we match the results against theoretical constraints on diagenetic alterations and discuss the effect of variable strain rates. Finally, we summarize our findings, compare them to accretionary wedge tectonics, and discuss possible implications for early stages of continental collision.

5.1. Tectonic Context and Relative Timing of Deformation Events

The earliest deformation in the IFUs can be expected to occur in a basinal setting. *Sinclair* [1989] documented different soft-sediment deformation features and interpreted them to form in the basin under the influence of the advancing thrust wedge and associated seismicity. We concur with this view and attribute the

sediment injections we observed to deformation in the basin, although an origin within the wedge cannot be excluded. Whether or not the injections were caused by seismic shaking cannot be solved here, but their occurrence documents at least overpressured pore fluids [e.g., *Levi et al.,* 2006]. The next tectonic event that can be expected to cause deformation is the imbrication of the flysch units. We argue that this is recorded by some of the deformation features that we documented within weakly deformed sediments. For example, deformation bands are a typical feature in argillaceous sediments drilled in the imbricate thrust zone of the Nankai accretionary prism, offshore Japan [e.g., *Karig and Lundberg*, 1990]. They occur in poorly cemented and compactively deforming sediments that exhibit a mixed brittle-ductile behavior ("ductile" refers to continuous deformation at the scale of observation, while "brittle" is used for discontinuous structures). Their formation is thought to record subhorizontal shortening induced by active accretion near the deformation front [e.g., *Karig and Lundberg*, 1990; *Morgan and Karig*, 1995, *Ujiie et al.*, 2004]. The deformation bands found in the IFUs share these principal characteristics. They developed in argillaceous sediments and record subhorizontal shortening as indicated by the reverse sense of shearing. Moreover, their association with small extension veins reflects a mixed brittle-ductile behavior of the sediments, where the veins record brittle rock failure and the deformation bands ductile shearing assisted by particulate flow. Such a mixed mechanical behavior is probably restricted to uncemented or poorly cemented sediments undergoing early stages of compaction [e.g., *Ask and Morgan*, 2010], as with progressive consolidation the elastic strength of sediments increases. We therefore suggest that the deformation bands in the IFUs record early phases of shortening during imbrication, similar to their counterparts in active accretionary wedges. This interpretation is in good agreement with independent observations. The small-scale folding of sediments together with G_1 calcite shear veins indicates bedding-parallel shortening and a mixed brittle-ductile behavior as well. *Dielforder et al.* [2015] determined low vein formation temperatures of only ~40–70°C, suggesting a very shallow origin for G_1 veins. In accordance with this, the veins are varyingly strong overprinted by sediment compaction, promoting their formation in a compacting environment.

Additional insights into deformation during imbrication can be obtained from the tectonic contacts between the different flysch units. For example, folding in the hanging wall of the imbricate thrusts is not associated with the formation of a tectonic cleavage, pressure solution, or crystal-plastic deformation. We further documented fault-propagation-folds within the Northhelvetic flysch (NHF) that also show no indications of pressure solution or crystal-plasticity. Similarly, *Gasser and den Brok* [2008] documented hectometer sized folds that again show no association with the aforementioned processes. These findings suggest that ductile deformation during folding was largely accommodated by particulate flow. We hypothesize that these folds formed in poorly consolidated sediments and record early phases of shortening during imbricate thrusting. The temperatures can be expected to be similar or slightly higher than the one for the formation of G_1 veins and related structures (i.e., $\geq$40–70°C). The poor consolidation of the sediments at these temperatures is supported by the inclusion of clays and fine-grained sediment particles in G_1 veins, which speaks against an origin in well-cemented rocks [e.g., *Orange et al.,* 1993; *Jeanbourquin*, 1994]. The suggested low temperatures for the folding of sediments during imbrication are in good agreement with observations from modern accretionary wedges. For example, geological surveys in submarine canyons that expose the internal architecture of the outer Nankai accretionary prism (Japan) revealed the folding of young turbidite sequences into trench parallel, hectometer-scaled folds [*Anma et al.,* 2011; *Hayman et al.*, 2011]. Similarly, *Yamamoto et al.* [2005] documented the folding of imbricated sediments into open to isoclinal folds in the Neogene Miura-Boso accretionary wedge, central Japan. The sediments never experienced temperatures above 50°C, which excludes any later stages of folding.

After imbrication of the flysch units, folding in the study area continued. This is recorded by the folding of the imbricate thrust faults [e.g., *Lihou*, 1996] and the local refolding of earlier folds [*Lihou*, 1996; *Gasser and den Brok*, 2008]. Previous studies argued that this regional folding event is related to the formation of an axial planar cleavage, based on the finding that the pressure solution cleavage is oriented subparallel to the axial planes of regional folds [e.g., *Milnes and Pfiffner*, 1977; *Lihou*, 1996]. Although we agree with the principle observation, we argue that folding and cleavage formation are not contemporaneous and interdependent processes, but only overlap partially in time. We documented that the pressure solution cleavage is heterogeneously developed within the study area. In the northern to central parts the cleavage is not developed, although the sediments are folded. In the southern part of the study area, the cleavage is well developed, especially in the Southhelvetic and Ultrahelvetic flysch. There, the cleavage is subparallel to bedding in the

long limbs of isoclinal folds and has a high angle to bedding within the fold hinges, consistent with the interpretation as axial planar cleavage. However, the formation of the pressure solution cleavage continued long after folding. For example, quartz-calcite veins in the southern part of the study area (G_2 and G_3 veins) formed after folding and crosscut early stages of the cleavage but are subsequently overprinted by ongoing pressure solution. As the veins formed at temperatures ≥200°C, the relationship suggests that folding occurred at temperatures below ~200°C, while pressure solution remained active (or became even more effective?) at temperatures ≥200°C. A similar relationship is also suggested by the isolated thrust slices in the north that record maximum temperatures of ~160–180°C. Pressure solution occurs only locally in these rocks (see section 3.1), but they were thrusted after regional folding of the IFUs. In this respect, we propose that folding and pressure solution are rather successive than contemporaneous processes, although they both record continuous shortening within the accreted flysch units. The comparable orientation of cleavage planes and axial planes simply suggests that the main shortening direction did not change significantly during their formation. As pressure solution continued after folding, it can be expected to tighten or to intensify folds and folding related fabrics. This expectation may be reflected by the structural appearance of disrupted strata within fold limbs (Figures 4d and 4e). We argue that the disruption initiated under progressive noncoaxial deformation and the rotation of the fold limbs into the extensional field [e.g., *Ramsay*, 1967]. After folding and disruption, continuous shortening perpendicular to the orientation of the fold limb resulted in pressure solution, which is displayed by the "flow" of the tectonic cleavage around boudinaged sandstone blocks (Figure 4d). In this respect, continuous pressure solution intensified the block in matrix fabric. In a similar way, we interpret the occurrence of mineralized tension gashes within hinge zone of folded sandstone layers to indicate a brittle overprint during late increments of shortening.

After imbrication and folding, the IFUs were affected by OOS-thrusting, which took place at temperatures between ~160–180°C and 300–320°C. Although OOS-thrusting in the study area is in the literature commonly associated with the activity of the Glarus thrust [e.g., *Ring et al.,* 2001], earlier phases of OOS-thrusting occurred and are recorded, e.g., by the emplacement of the Subhelvetic units on top of the IFUs (see section 2.2). We suggest that the flysch internal thrust faults developed during the same period. Our interpretation is based on the structural appearance of the thrust faults. In contrast to the imbricate thrust faults that exhibit only a weak brittle overprint in the foot and hanging wall and are associated with a calcite mineralization, the flysch internal thrust faults exhibit intense brittle fracturing and a mineralization by quartz, calcite, and minor amounts of chlorite and white mica. The persistence of a quartz-calcite mineralization is recorded by the G_2 and G_3 veins for temperatures of ~200–300°C (see above) [*Dielforder et al.,* 2015], suggesting similar temperature ranges for the activity of the thrust faults. Moreover, the mineral veins overprint well-cemented and compacted sediments excluding an early origin for the faults. We further reject a retrograde origin, as the fault structure is overprinted by open clefts formed during exhumation.

5.2. Effects of Diagenesis on Deformation

In the following, we examine the potential effects of diagenetic alterations and changing sediment properties on deformation within the IFUs. For this purpose, we compare the calculated depth and temperature intervals for sediment compaction and clay dehydration (Figure 7) with the temperature ranges of different deformation events. The results are projected on the depth-temperature path obtained from equation (4) (Figure 8; see section 4). Our calculations suggest that the porosity decreases from 60% to ~10% within the upper ~5 km of the wedge (Figure 8a). Similarly, the illitization of smectite initiates at a depth of ~3–4 km and peaks around ~4–6 km depth or temperatures of ~100°C (Figures 7a and 8a). The largest amounts of fluids are thus liberated within the upper ~6 km of the wedge, which is reflected in the relatively high values of the bulk fluid source term Γ_{bulk}, where $\Gamma_{bulk} = \Gamma_{com} + \Gamma_{clay}$ (Figures 7 and 8a). Both illitization and sediment compaction remain active until depths of ~10 km, at which the residual porosity becomes less than 2% and temperatures reach ~170°C. Although both processes continuously release further fluids, the bulk fluid source term is 1 order of magnitude smaller than at shallower depths (Figure 8a). In summary, the model results suggest that sediment compaction and illitization completed in the IFUs within the upper ~5–10 km of the wedge. *Dielforder et al.* [2015] further proposed on the basis of isotope analysis of calcite cements from marl and limestones that carbonate diagenesis in the IFUs occurred at temperatures of ~40–70°C or depths of ~3–4 km (Figure 8a). The diagenetic reactions, i.e., carbonate diagenesis and the smectite-illite transformation, release cations like Ca^{2+}, Mg^{2+}, Fe^{3+}, and Si^{4+} into the pore fluid, which fosters the cementation of the sediments [e.g., *Sample*, 1990;

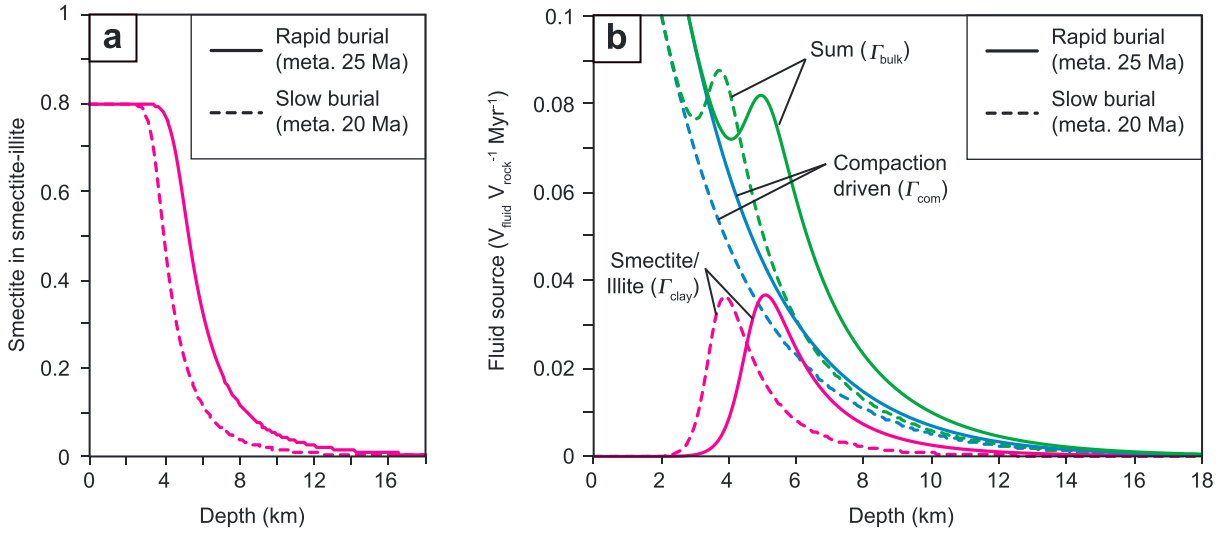

Figure 7. (a) Model results showing the smectite content in mixed smectite-illite as a function of depth. (b) Calculated fluid source terms for sediment compaction (Γ_{com}), smectite-illite transformation (Γ_{clay}), and the sum of both (bulk fluid source term, Γ_{bulk}). Dashed and solid lines represent model results for metamorphism in the Infrahelvetic flysch units at 20 Ma and 25 Ma, respectively. For details on the calculations see section 4.

Awwiller, 1993; *Moore et al.,* 2007]. We therefore suggest that the originally unconsolidated and soft sediments were transferred into cemented and rigid rocks within the upper ~10 km of the wedge. We argue that this diagenetic embrittlement is reflected by the restriction of imbricate thrusting and associated folding to temperatures below ~160°C (Figures 8b and 8c). In this respect, the originally unconsolidated state of the sediments enabled ductile deformation by particulate flow especially within the upper kilometers of the wedge. With the progressive diagenetic alteration of the sediments, particulate flow became more difficult and finally ceased at deeper levels of the wedge. The exact temperature range for the switch in the mechanical behavior is difficult to constrain and may vary within the wedge. For example, the strong compaction of sediments together with the associated fluid release promote high pore fluid pressures [e.g., *Wang*, 1994; *Moore and Saffer*, 2001], which are likely to cause an underconsolidation of the sediments and low effective stresses within the wedge. Such a setting would extend the effective depth range for deformation by particulate flow [e.g., *Borradaile*, 1981; *Ask and Morgan*, 2010].

At depths greater than ~10 km, the porosity remains approximately stable (i.e., around the fixed minimum porosity of 1%) and illite is progressively transformed into muscovite [e.g., *van de Kamp*, 2008]. Compared to earlier deformation stages, the liberation of fluids at this stage is rather negligible as indicated by the low values of Γ_{bulk} (Figure 8a). At the same depths, however, pressure solution becomes active and causes together with the illite-muscovite transformation the liberation and redistribution of SiO_2, which is thought to facilitate a further embrittlement of the rocks and the change from a velocity-strengthening to velocity-weakening behavior [e.g., *Moore et al.,* 2007; *van de Kamp*, 2008; *Kameda et al.,* 2014]. We propose that this development is reflected by the onset of OOS-thrusting at temperature >160°C and the brittle deformation that is recorded by the formation of quartz-calcite veins in the study area (Figure 8b).

5.3. Effects of Strain Rate on Deformation

At first glance, our data set documents an overall mechanical embrittlement that is linked to the prograde diagenetic alteration of the IFUs. At second sight, however, the data display also the formation of brittle and ductile deformation features under comparable diagenetic conditions. Especially at early diagenetic states, such differences might be caused by inhomogeneous lithification and variable pore fluid pressures [e.g., *Labaume*, 1987; *Ortner*, 2007]. Besides, a variation of the strain rate adds another major control on the mechanical behavior of the sediments and is discussed in the following. Strain partitioning in the imbricate thrust zone can cause highly variable strain rates at different sites in the accreted sediments [e.g., *Barnes et al.,* 1998]. The highest strain rates occur along the plate boundary fault and imbricate thrusts that accommodate large amount of plate convergence, while lower strain rates can be expected for the interior of the imbricated

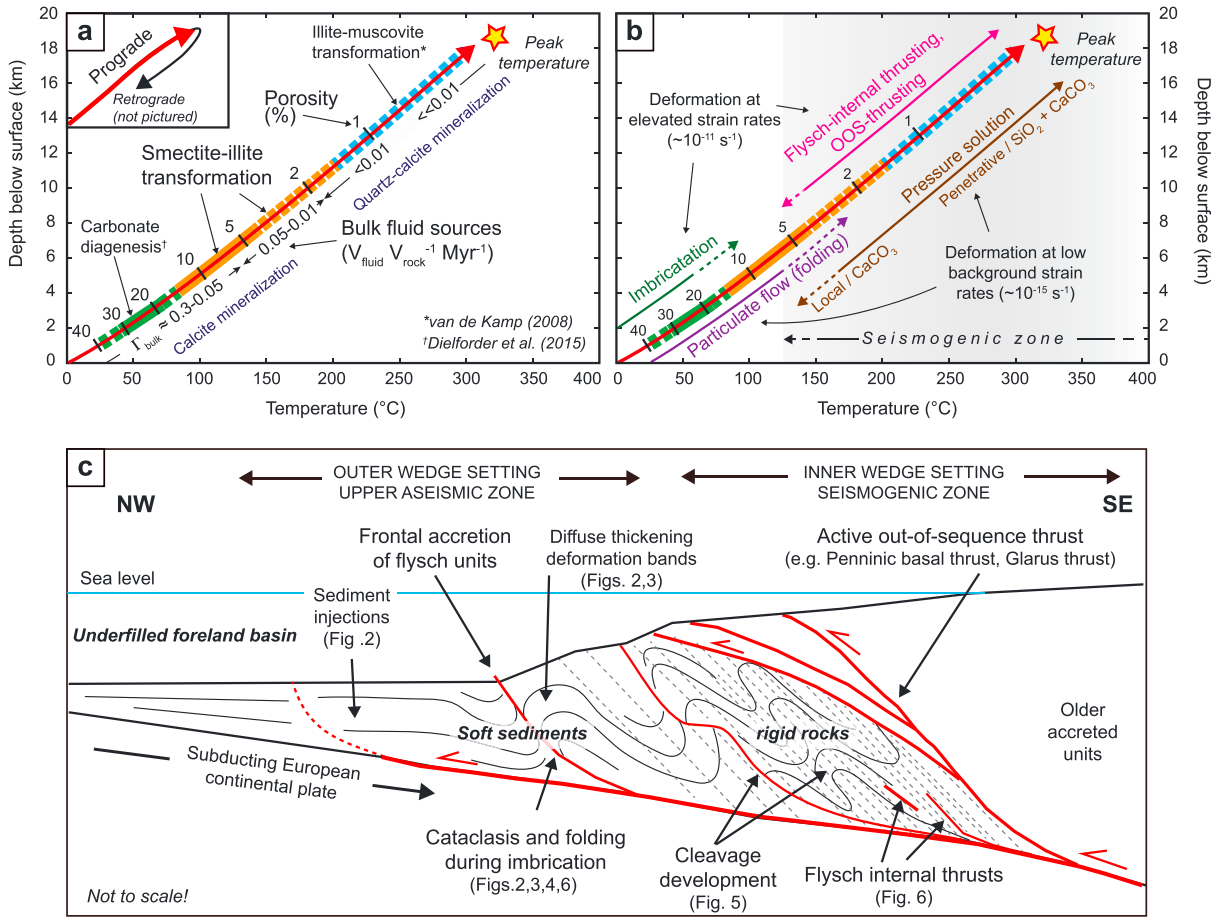

Figure 8. (a) Diagram illustrating the computed thermal profile, porosity structure and depths of diagenetic alterations as inferred for the prograde evolution of the Infrahelvetic flysch units. The depths of carbonate diagenesis, smectite-illite-, and illite-muscovite transformation are given by the green, orange, and blue boxes, respectively. Computed porosities are given by black ticks and the numbers above the temperature curve. The bulk fluid source term (Γ_{bulk}) is given by the numbers below the temperature curve. (b) Diagram as in Figure 8a but showing the range of different tectonic processes as inferred from field observations (see text for explanation). (c) Schematic tectonic model for the accretion of underfilled foreland basin sediments during early stages of continental collision. The basin sediments are frontally accreted in an unconsolidated state. Folding initiates already during imbrication. Active out-of-sequence thrusting in the rearward part of the wedge results in the tectonic burial of the accreted units. At greater depths the sediments experience diagenesis and low metamorphism and are transformed into rigid rocks. Folds and folding related structures are overprinted by a pressure solution cleavage. For details on the calculations see section 4.

units [e.g., *Adam et al.,* 2005]. Although the strain rates during imbrication of the IFUs are difficult to reconstruct, a first-order approximation may illustrate potential differences. For example, presuming that one third of plate convergence (i.e., ~2–4 mm yr^{-1}, see section 4.2) was taken up along the imbricate thrust faults within a ~1 m thick shear zone, yields a bulk strain rate of ~10^{-11} s^{-1}. In contrast, folding in the interior of the IFUs records roughly 20–40% of shortening [*Lihou*, 1996]. Considering that most of the folding occurred during imbrication, i.e., within ~5 Myr, suggests low bulk strain rates for folding at the order of ~10^{-14}–10^{-15} s^{-1} [see also *Milnes and Pfiffner*, 1977]. In summary, strain rates in the IFUs may have varied by a minimum of 3 to 4 orders of magnitude. In this respect, the cataclasites and mineral veins that are associated with the imbricate thrusts record brittle and frictional deformation in a high strain zone, while the ductile folding of sediments reflects continuous shortening at low background strain rates. Similarly, the occurrence of early formed mineral veins together with small-scale folds is also likely to reflect variations in the strain rate. *Dielforder et al.* [2015] suggested that the G_1 veins record rock failure in response to subduction earthquakes that cause a coseismic contraction of the outer wedge. This implies that the mineral veins formed during short periods of elevated strain rates, while the small-scale folding reflect deformation at lower background strain rates, analogous to the larger folds. After folding or at temperatures >160°C, the low background strains were progressively accommodated by spatially wide distributed pressure solution, which remained

active until peak metamorphic conditions and caused the intensification of the rock fabric (see section 3.3). The resultant "ductile appearance" of the rocks probably motivated previous workers to subsume thrusting, folding, and cleavage formation under the D_2 Alpine deformation phase, expressing the idea that the IFUs experienced high ductile and penetrative strains, as inferred, e.g., for the Helvetic Morcles nappe in western Swiss Alps [*Ramsay and Huber*, 1983; *Egli and Mancktelow*, 2013]. However, the low background strain rates associated with pressure solution account only for small total strains. Moreover, the actual brittle behavior of the rocks at late stages of the prograde evolution is well expressed by the brittle fracturing and the formation of quartz-calcite veins. Similarly, the flysch internal thrust faults and the OOS-thrusts record the brittle accommodation of shortening at much higher rates than the background strain rate. For example, the Glarus thrust accommodated a minimum of ~30 km slip within ~10 Myr [e.g., *Schmid*, 1975; *Pfiffner*, 1985]. This translates to average strain rates of 7×10^{-11} to $1 \times 10^{-10}\,s^{-1}$ or slip rates of ~2–4 mm yr^{-1}, suggesting that ~30–50% of plate convergence were taken up along the fault. We note that the Glarus thrust was previously interpreted as ductile shear zone, due to a ~1–2 m thick calc-mylonite that occurs in the direct footwall of the thrust [e.g., *Schmid*, 1975; *Ebert et al.,* 2007; *Herwegh et al.,* 2008]. However, the fault shows a clear discontinuous offset and the required high strain rates of $\sim 10^{-11}\,s^{-1}$ in combination with comparable low temperatures of only ~200–350°C do not speak for a sole ductile accommodation of the overall displacement. On the contrary, discrete slip surfaces and cataclasites in the calc-mylonite suggest that considerable amounts of the displacement were taken up in a brittle manner, while the crystal-plastic deformation in the calc-mylonite reflects deformation at low background strain rates, analogous to pressure solution in the underlying flysch units [*Badertscher and Burkhard*, 2000]. This view is supported by a recent chemomechanical model for the Glarus thrust that implements frictional stick-slip failure in an otherwise (interseismically) plastically deforming calc-mylonite [*Poulet et al.,* 2014].

5.4. Similarities to Accretionary Wedges and Implications for Early Stages of Continental Collision

Our study documents that the early stages of tectonic deformation affected soft sediments and were related to the imbrication of the IFUs. At this stage, bedding-parallel shortening, folding, and stratal disruption initiated and were accompanied by the formation of smaller-scale structures like deformation bands or bedding-parallel shear veins. The inferred low diagenetic conditions suggest a setting at a very shallow level within the young Alpine wedge. We interpret these characteristics to reflect frontal accretion of the flysch units rather than underthrusting and subsequent basal accretion (Figure 8c). After frontal accretion, the diagenetic alteration of the sediments increased their elastic strength and resulted in an overall mechanical embrittlement. At deeper levels of the wedge, deformation at elevated strain rates was localized along brittle thrust faults, like flysch-internal thrusts or orogen-scale OOS-thrusts that promoted the tectonic burial of the accreted flysch units. In contrast, lower background strain was accommodated by pressure solution resulting in the formation of a pervasive cleavage (Figure 8c).

The inferred tectonic and structural evolution shows similarities to the one of accretionary wedges that form at accretion-dominated subduction zones, like along the North and South American margins or the Japan Trench [*Moore et al.,* 2007, and references therein]. Such accretionary complexes are commonly divided into an outer and inner wedge [e.g., *Wang and Hu*, 2006]. The outer wedge encompasses the imbricate thrust zone, where poorly lithified sediments are accreted in sequence to the front of the prism. Stratal disruption, folding, and the formation of compaction bands have been documented as typical features in many active and fossil outer wedges [e.g., *Sample*, 1990; *Orange et al.,* 1993; *Morgan and Karig*, 1995; *Vannucchi and Bettelli*, 2002; *Yamamoto et al.,* 2005; *Moore et al.,* 2007; *Kimura et al*., 2012]. In contrast, the inner wedge represents the interior part of an accretionary complex. It comprises well-lithified sediments and is characterized by OOS-thrusting, underplating, widespread pressure solution, quartz cementation, and massive quartz-calcite veining, i.e., all processes that we also infer for the late stage evolution of the IFUs [e.g., *Sample and Moore*, 1987; *Schwartz and Stöckhert*, 1996; *Ring and Brandon*, 1999; *Park et al.*, 2002; *Moore et al.,* 2007].

The similarities between the two systems suggest that the "accretionary wedge stage" of the evolving Alpine orogen continued after the subduction of the Valais trough (or North Penninic ocean, see section 2). This finding bears some implications for the tectonics during early stages of continental collision, which we discuss briefly in the following. The tectonics of accretionary wedges is strongly dominated by two factors. The first factor is a switch in the mechanical behavior of the sediments from a velocity-weakening to a velocity-strengthening rheology. This switch is caused by the diagenetic alteration of the sediments, takes place at

temperatures of ~125–150°C, and falls together with the transition from the outer to the inner wedge as well as with the onset of seismogenesis [e.g., *Moore and Saffer*, 2001; *Wang and Hu*, 2006]. The second factor is the high pore fluid pressure within the wedge, which is caused by mineral dehydration, rapid sediment compaction, and low permeabilities [e.g., *Saffer and Tobin*, 2011]. These two factors determine how plate convergence is taken up and strain is localized. For instance, OOS-thrusts have been identified as a map-scale example of seismogenic thrust faults that splay from the plate boundary fault and cut through the entire inner wedge [e.g., *Moore et al.,* 2007; *Strasser et al.,* 2009; *Lieser et al.,* 2014]. Slip on OOS-thrusts may be activated by large subduction earthquakes on the plate boundary fault [e.g., *Lieser et al.,* 2014]. Moreover, OOS-thrusts in the Nankai accretionary prism are characterized by alternating periods of low and high activity [*Strasser et al.,* 2009]. During phases of high activity the thrusts accommodate significant portions of plate convergence, while it is taken up by in sequence imbrication at the front of wedge during periods of low activity [*Strasser et al.,* 2009; *Tsuji et al*., 2014]. This dynamic picture offers a new perspective on the tectonic evolution of the Alpine orogenic front. Both the Penninic basal thrust and Helvetic basal thrusts (e.g., Glarus thrust, Figures 1 and 8c) can be understood as analogon to OOS-thrusts in accretionary wedges, which were active within the seismogenic part of the Alpine wedge. We propose therefore that the frontal accretion of the different flysch units and OOS-thrusting along the Penninic or at a later stage along the Glarus thrust represent alternating periods, during which plate convergence was either accommodated by frontal accretion or by OOS-thrusting. In this respect, the emplacement of the Helvetic nappes along the Glarus thrust is rather an example for the growth of accretionary complexes at convergent margins than a specific example for collisional tectonics.

Another aspect are the high pore fluid pressures that persist within fault zones and large parts of accretionary wedges [e.g., *Moore and Saffer*, 2001; *Tobin and Saffer*, 2009; *Moreno et al.,* 2014; *Tsuji et al.,* 2014]. The overpressures keep the effective stresses and hence strength of the fault and the surroundings low, which promotes the subduction of the oceanic slab [e.g., *Lamb*, 2006; *Seno*, 2009; *Hardebeck*, 2015]. We propose that similar low-stress conditions persisted on the basal detachment and on out-of-sequence-thrusts throughout the prograde evolution of the IFUs. Our interpretation is in accordance with independent constraints presented by *Ring et al.* [2001], who suggested low stresses on the Glarus thrust based on finite strain measurements within the footwall and hanging wall of the fault. Considering that the elevation of a mountain range approximately relates to the shear stress on the plate boundary fault [*Lamb and Davis*, 2003; *Lamb*, 2006], we further hypothesize that the proposed steady state advance of the submarine Alpine wedge during early stages of continental collision was at least partially facilitated by low shear stresses on the plate boundary. In this respect, the prograde tectonic evolution of the IFUs was rather characterized by continental subduction than by continental collision.

In summary, our findings and interpretations underline the impact of unlithified, fine-grained siliciclastic sediments on mountain building processes. As underfilled foreland basins are a typical feature of collision zones, we suppose that our results bear also significance for better understanding the tectonic evolution of other orogens, like the Apennines, Himalaya, Zagros, or the Burmese Wedge. Moreover, the link to accretionary wedge tectonics may motivate to consider more the unique and manifold insights from active convergent plate margins in the analysis of fossil collision zones.

6. Conclusions

We reconstructed the prograde tectonic evolution of the Infrahelvetic flysch units within the geodynamic context of incipient continental collision and associated inversion of an underfilled foreland basin. Our study suggests that the tectonic incorporation of the IFUs resembles the formation and growth of accretionary wedges that form at subduction zones. In this respect, the frontal Alpine wedge can be divided into an outer and an inner wedge. The outer wedge comprises the imbricate thrust zone, in which unlithified foreland basin sediments were frontally accreted. The inner wedge, in turn, represents the more interior and deeper levels, which were characterized by out-of-sequence thrusting, pervasive pressure solution, and quartz-calcite veining. Pore fluid pressures were presumably very high and kept the effective stresses along thrust faults and the interior of the wedge low. Plate convergence was therefore accommodated along the plate boundary fault and out-of-sequence thrusts. We suppose that this setting allowed the underthrusting or subduction of 150–200 km of European continental crust. Throughout this evolution, the European plate

was not (or only at deeper levels of the wedge) involved in deformation. This changed during the retrograde evolution, which was characterized by thrusting, shearing, and exhumation of the Aar massif. We suppose that the strength of the former basal detachment significantly increased during this time, promoting the relocalization of deformation into the crystalline crust. The factors causing the switch in the tectonic style have remained largely elusive and are topic of future research.

Acknowledgments
Funding for this project was provided by the Swiss National Science Foundation (144381). We thank R.M. Danisi and M. Peters for discussion. We are grateful for the comments by the Associate Editor P. Vannucchi, one anonymous reviewer, and P. Labaume, which helped us to greatly improve on the original manuscript. The data for this paper are available by contacting the corresponding author (armin@crpg.cnrs-nancy.fr). The results of the XRD measurements are provided in the supporting information.

References

Adam, J., J. L. Urai, B. Wieneke, O. Oncken, K. Pfeiffer, N. Kukowski, J. Lohrmann, S. Hoth, W. van der Zee, and J. Schmatz (2005), Shear localization and strain distribution during tectonic faulting—New insights from granular-flow experiments and high-resolution optical image correlation techniques, *J. Struct. Geol.*, *27*, 283–301.

Allen, P. A., P. Homewood, and G. D. Williams (1986), Foreland Basins: An introduction, in *Foreland Basins*, *Spec. Publs. Int. Ass. Sediment*., vol. 8, edited by P. A. Allen and P. Homewood, pp. 3–12, Blackwell Scientific, Oxford.

Anma, R., et al. (2011), Structural profile and development of the accretionary complex in the Nankai trough, southwest Japan: Results of submersible studies, in *Accretionary Prisms and Convergent Margin Tectonics in the Northwest Pacific Basin*, edited by Y. Ogawa et al., pp. 169–196, Springer, New York.

Ask, M. V. S., and J. K. Morgan (2010), Projection of mechanical properties from shallow to greater depths seaward of the Nankai accretionary prism, *Tectonophysics*, *482*, 50–64.

Awwiller, D. N. (1993), Illite/smectite formation and potassium mass transfer during burial diagenesis of mudrocks: A study from the Texas gulf coast Paleocene-Eocene, *J. Sediment. Petrol.*, *63*, 501–512.

Badertscher, N. P., and M. Burkhard (2000), Brittle-ductile deformation in the Glarus thrust Lochseiten (LK) calc-mylonite, *Terra Nova*, *12*, 281–288.

Barnes, P. M., B. M. de Lépinay, J.-Y. Callot, J. Delteil, and J.-C. Audru (1998), Strain partitioning in the transition area between oblique subduction and continental collision, Hikurangi margin, New Zealand, *Tectonics*, *17*, 534–557, doi:10.1029/98TC00974.

Beaumont, C. (1981), Foreland basins, *Geophys. J. R. Astron. Soc.*, *65*, 291–329.

Borradaile, G. J. (1981), Particulate flow of rock and the formation of cleavage, *Tectonophysics*, *72*, 305–321.

Bray, C. J., and D. E. Karig (1985), Porosity of sediments in accretionary prisms and some implications for dewatering processes, *J. Geophys. Res.*, *90*, 768–778, doi:10.1029/JB090iB01p00768.

Burkhard, M. (1990), Aspects of the large-scale Miocene deformation in the most external part of the Swiss Alps (Subalpine Molasse to Jura fold belt), *Eclogae Geol. Helv.*, *83*, 559–583.

Colten-Bradley, V. A. (1987), Role of pressure in smectite dehydration: Effects of geopressures and smectite-illite transformation, *Am. Pet. Geol. Bull.*, *71*, 1414–1427.

Davies, J. H. (2013), Global map of solid Earth surface heat flow, *Geochem. Geophys. Geosyst.*, *14*, 4608–4622, doi:10.1002/gggge.20271.

Dewey, J. F., and J. M. Bird (1970), Mountain belts and the new global tectonics, *J. Geophys. Res.*, *75*, 2625–2647, doi:10.1029/JB075i014p02625.

Dielforder, A., H. Vollstaedt, T. Vennemann, A. Berger, and M. Herwegh (2015), Linking megathrust earthquakes to brittle deformation in a fossil accretionary complex, *Nat. Commun.*, *6*, 7504, doi:10.1038/ncomms8504.

Ebert, A., M. Herwegh, and A. Pfiffner (2007), Cooling induced strain localization in carbonate mylonites within a large-scale shear zone (Glarus thrust, Switzerland), *J. Struct. Geol.*, *29*, 1164–1184.

Egli, D., and N. Mancktelow (2013), The structural history of the Mont Blanc massif with regard to models for its recent exhumation, *Swiss J. Geosci.*, *106*, 469–489.

Festa, A., G. A. Pini, Y. Dilek, and G. Codegone (2010), Mélanges and mélange-forming processes: A historical overview and new concepts, *Int. Geol. Rev.*, *52*, 1040–1105.

Frey, M. (1988), Discontinuous inversed metamorphic zonation, Glarus Alps, Switzerland: Evidence from illite crystallinity data, *Schweiz. Mineral. Petrogr. Mitt.*, *86*, 171–184.

Frey, M., M. Teichmüller, R. Teichmüller, J. Mullis, B. Künzi, A. Breitschmid, U. Gruner, and B. Schwizer (1980), Very low grade metamorphism in external parts of the Central Alps: Illite crystallinity, coal rank and fluid inclusion data, *Eclogae Geol. Helv.*, *73*, 173–203.

Frisch, W. (1979), Tectonic progradation and plate tectonic evolution of the Alps, *Tectonophysics*, *60*, 121–139.

Garcia-Castellanos, D., and S. Cloetingh (2012), Modeling the interaction between lithospheric and surface processes in foreland basins, in *Tectonics of Sedimentary Basins: Recent Advances*, edited by C. Busby and A. Azor, pp. 152–181, Blackwell Publishing, Oxford.

Gasser, D., and B. den Brok (2008), Tectonic evolution of the Engi Slates, Glarus Alps, Switzerland, *Swiss J. Geosci.*, *101*, 311–322.

Glotzbach, C., J. Reinecker, M. Danišík, M. Rahn, W. Frisch, and C. Spiegel (2010), Thermal history of the central Gotthard and Aar massifs, European Alps: Evidence for steady state long-term exhumation, *J. Geophys. Res.*, *115*, F03017, doi:10.1029/2009JF001304.

Handy, M. R., S. M. Schmid, R. Bousquet, E. Kissling, and D. Bernoulli (2010), Reconciling plate-tectonic reconstructions of Alpine Tethys with the geological-geophysical record of spreading and subduction in the Alps, *Earth Sci. Rev.*, *102*, 121–158.

Hardebeck, J. L. (2015), Stress orientations in subduction zones and the strength of subduction megathrusts, *Science*, *349*, 1213–1216.

Hayman, N. W., K. C. Burmeister, K. Kawamura, R. Anma, and Y. Yamada (2011), Submarine outcrop evidence for transpressional deformation within the Nankai accretionary prism, Tenryu canyon, Japan, in *Accretionary Prisms and Convergent Margin Tectonics in the Northwest Pacific Basin*, edited by Y. Ogawa et al., pp. 197–214, Springer, New York.

Herwegh, M., and O. A. Pfiffner (2005), Tectono-metamorphic evolution of a nappe stack: A case study of the Swiss Alps, *Tectonophysics*, *404*, 55–76.

Herwegh, M., J.-P. Hürzeler, O. A. Pfiffner, S. M. Schmid, R. Abart, and A. Ebert (2008), The Glarus thrust: Excursion guide and report of a field trip of the Swiss Tectonic Studies Group (Swiss Geological Society, 14.–16.09.2006), *Swiss J. Geosci.*, *101*, 323–340.

Hunziker, J. C., M. Frey, N. Clauer, R. D. Dallmeyer, H. Friedrichsen, W. Flehmig, K. Hochstrasser, P. Roggwiler, and H. Schwander (1986), The evolution of illite to muscovite; mineralogical and isotopical data from the Glarus Alps, Switzerland, *Contrib. Mineral. Petrol.*, *92*, 157–180.

Hyndman, R. D., and K. Wang (1993), Thermal constraints on the zone of major thrust earthquake failure: The Cascadia Subduction zone, *J. Geophys. Res.*, *98*, 2039–2060, doi:10.1029/92JB02279.

Jeanbourquin, P. (1994), Early deformation of Ultrahelvetic mélanges in the Helvetic nappes (western Swiss Alps), *J. Struct. Geol.*, *16*, 1367–1383.

Jordan, T. E. (1981), Thrust loads from foreland basin evolution, Cretaceous, western United States, *Am. Assoc. Pet. Geol. Bull.*, *65*, 2560–2520.

Kameda, J., K. Kawabata, Y. Hamada, A. Yamaguchi, and G. Kimura (2014), Quartz deposition and its influence on the deformation process of megathrusts in subduction zones, *Earth Planets Space*, *66*, 13, doi:10.1186/1880-5981-66-13.
Karig, D. E., and N. Lundberg (1990), Deformation bands from the toe of the Nankai accretionary prism, *J. Geophys. Res.*, *95*, 9099–9109, doi:10.1029/JB095iB06p09099.
Kempf, O., and O. A. Pfiffner (2004), Early Tertiary evolution of the North Alpine Foreland Basin of the Swiss Alps and adjoining areas, *Basin Res.*, *16*, 549–567.
Kimura, G., et al. (2007), Transition of accretionary wedge structures around the up-dip limit of the seismogenic subduction zone, *Earth Planet. Sci. Lett.*, *255*, 471–484.
Kimura, G., et al. (2012), Tectonic mélange as fault rock of subduction plate boundary, *Tectonophysics*, *568–569*, 25–38.
Koehn, D., and C. W. Passchier (2000), Shear sense indicators in striped-bedding veins, *J. Struct. Geol.*, *22*, 1141–1151.
Labaume, P. (1987), Syn-diagenetic deformation of a turbiditic succession related to submarine gravity nappe emplacement, Autapie Nappe, French Alps, in *Deformation of Sediments and Sedimentary Rocks*, *Spec. Publs*., vol. 29, edited by M. E. Jones and R. M. F. Preston, pp. 147–164, Geol. Soc., London.
Labaume, P., C. Berty, and P. Laurent (1991), Syn-diagenetic evolution of shear structures in superficial nappes: An example from the Northern Apennines (NW Italy), *J. Struct. Geol.*, *18*, 385–398.
Lahfid, A., O. Beyssac, E. Deville, F. Negro, C. Chopin, and B. Goffé (2010), Evolution of the Raman spectrum of carbonaceous material in low-grade metasediments of the Glarus Alps (Switzerland), *Terra Nova*, *22*, 354–360.
Lamb, S. (2006), Shear stresses on megathrusts: Implications for mountain building behind subduction zones, *J. Geophys. Res.*, *111*, B07401, doi:10.1029/2005JB003916.
Lamb, S., and P. Davis (2003), Cenozoic climate change as possible cause for the rise of the Andes, *Nature*, *425*, 792–797.
Lauer, R. M., and D. M. Saffer (2015), The impact of splay faults on fluid flow, solute transport, and pore pressure distribution in subduction zones: A case study offshore the Nicoya Peninsula, Costa Rica, *Geochem. Geophys. Geosyst.*, *16*, 1089–1104, doi:10.1002/2014GC005638.
Levi, T., R. Weinberger, T. Aifa, Y. Eyal, and S. Marco (2006), Earthquake-induced clastic dikes detected by anisotropy of magnetic susceptibility, *Geology*, *34*, 69–72.
Lieser, K., I. Grevemeyer, D. Lange, E. Flueh, F. Tilmann, and E. Contreras-Reyes (2014), Splay fault activity revealed by aftershocks of the 2010 M_w 8.8 Maule earthquake, central Chile, *Geology*, *42*, 823–826.
Lihou, J. (1996), Structure and deformational history of the Infrahelvetic flysch units, Glarus Alps, eastern Switzerland, *Eclogae Geol. Helv.*, *89*, 439–460.
Maltman, A. (1994), Introduction and overview, in *The Geological Deformation of Sediments*, edited by A. Maltman, pp. 1–36, Chapman & Hall, London.
Milnes, A. G., and O. A. Pfiffner (1977), Structural development of the Infrahelvetic complex, eastern Switzerland, *Eclogae Geol. Helv.*, *70*, 83–95.
Mohn, G., G. Manatschal, M. Beltrando, and I. Haupert (2014), The role of rift-inherited hyper-extension in Alpine-type orogens, *Terra Nova*, *26*, 347–352.
Molnar, P., and P. England (1990), Temperatures, heat flux, and frictional stress near major thrust faults, *J. Geophys. Res.*, *95*, 4833–4856, doi:10.1029/JB095iB04p04833.
Moore, J. C., and D. M. Saffer (2001), Updip limit of the seismogenic zone beneath the accretionary prism southwest Japan: An effect of diagenetic to low-grade metamorphic processes and increasing effective stress, *Geology*, *29*, 183–186.
Moore, J. C., and P. Vrolijk (1992), Fluids in accretionary prisms, *Rev. Geophys.*, *30*, 113–135, doi:10.1029/92RG00201.
Moore, J. C., C. Rowe, and F. Meneghini (2007), How accretionary prisms elucidate seismogenesis in subduction zones, in *The Seismogenic Zone of Subduction Thrust Faults*, edited by T. H. Dixon and J. C. Moore, pp. 288–315, Columbia Univ. Press, New York.
Moreno, M., C. Haberland, O. Oncken, A. Rietbrock, S. Angiboust, and O. Heidbach (2014), Locking of the Chile subduction zone controlled by fluid pressure before the 2010 earthquake, *Nat. Geosci.*, *7*, 292–296.
Morgan, J. K., and D. E. Karig (1995), Kinematics and a balanced and restored cross-section across the toe of the eastern Nankai accretionary Prism, *J. Struct. Geol.*, *17*, 31–45.
Oncken, O., C. von Winterfeld, and U. Dittmar (1999), Accretion of a rifted passive margin: The Late Paleozoic Rhenohercynian fold and thrust belt (Middle European Variscides), *Tectonics*, *18*, 75–91, doi:10.1029/98TC02763.
Orange, D. L., D. S. Geddes, and J. C. Moore (1993), Structural and fluid evolution of a young accretionary complex: The Hoh rock assemblage of the western Olympic Peninsula, Washington, *Geol. Soc. Am. Bull.*, *105*, 1053–1075.
Ortner, H. (2007), Styles of soft-sediment deformation on top of a growing fold system in the Gosau Group at Muttenkopf in the Northern Calcareous Alps, Austria: Slumpings versus tectonic deformation, *Sediment. Geol.*, *196*, 99–118.
Ortner, H., S. Aichholzer, M. Zerlauth, R. Pilser, and B. Fügenschuh (2015), Geometry, amount, and sequence of thrusting in the Subalpine Molasse of Western Austria and Southern Germany, European Alps, *Tectonics*, *34*, 1–30, doi:10.1002/2014TC003550.
Passchier, C. W., and R. A. Trouw (2005), *Microtectonics*, 2nd ed., pp. 366, Springer, Heidelberg, Berlin.
Pelletier, J. D. (2007), Erosion-rate determination from foreland basin geometry, *Geology*, *35*, 5–8.
Pfiffner, A. O. (1985), Displacements along thrust faults, *Eclogae Geol. Helv.*, *78*, 313–333.
Pfiffner, A. O. (1986), Evolution of the north Alpine foreland basin in the central Alps, in *Foreland Basins*, *Spec. Publs. Int. Ass. Sediment*., vol. 8, edited by P. A. Allen and P. Homewood, pp. 219–228, Blackwell Scientific, Oxford.
Pfiffner, O. A. (2011), Structural Map of the Helvetic Zone of the Swiss Alps, including Vorarlberg (Austria) and Haute Sovie (France), 1:100000, *Geological Special Map*. Swisstopo, Wabern.
Pollack, N. H. (1982), The heat flow from the continents, *Ann. Rev. Earth Planet. Sci.*, *10*, 459–481.
Poulet, T., M. Veveakis, M. Herwegh, T. Buckingham, and K. Regenauer-Lieb (2014), Modeling episodic fluid-release events in the ductile carbonates of the Glarus thrust, *Geophys. Res. Lett.*, *41*, 7121–7128, doi:10.1002/2014GL061715.
Pytte, A. M., and R. C. Reynolds (1988), The thermal transformation of smectite to illite, in *Thermal History of Sedimentary Basins*, edited by N. D. Naeser and T. H. McCulloh, pp. 133–140, Springer, Berlin.
Rahn, M. K., and B. Grasemann (1999), Fission track numerical thermal modeling of differential exhumation of the Glarus thrust plane (Switzerland), *Earth Plant. Sci. Lett.*, *169*, 245–259.
Rahn, M. K., A. J. Hurford, and M. Frey (1997), Rotation and exhumation of a thrust plane: Apatite fission-track data from the Glarus thrust, Switzerland, *Geology*, *25*, 599–602.
Rahn, M., J. Mullis, and K. Erdelbrock (1995), Alpine metamorphism in the North Helvetic Flysch of the Glarus Alps, Switzerland, *Eclogae Geol. Helv.*, *88*, 157–178.

Ramsay, J. G. (1967), *Folding and Fracturing of Rocks*, pp. 568, McGraw-Hill, New York.
Ramsay, J. G., and M. I. Huber (1983), *The Techniques of Modern Structural Geology, Volume 1: Strain Analysis*, pp. 307, Academic Press, London.
Remitti, F., G. Bottelli, and P. Vannucchi (2007), Internal structure and tectonic evolution of an underthrust tectonic mélange: The Sestola-Vidiciatico tectonic unit of the northern Apennines, Italy, *Geodin. Acta*, *20*, 37–51.
Ring, U., and M. T. Brandon (1999), Ductile deformation as mass loss in the Franciscan Subduction-Complex: Implication for exhumation processes in accretionary wedges, in *Exhumation Processes, Normal Faulting, Ductile Flow, and Erosion*, edited by U. Ring et al., pp. 55–86, Geol. Soc, London.
Ring, U., M. T. Brandon, and A. Ramthun (2001), Solution-mass-transfer adjacent to the Glarus Thrust, with implication to the tectonic evolution of the Alpine wedge in eastern Switzerland, *J. Struct. Geol.*, *23*, 1491–1505.
Saffer, D. M. (2003), Pore pressure development and progressive dewatering in underthrust sediments at the Costa Rican subduction margin: Comparison with northern Barbados and Nankai, *J. Geophys. Res.*, *108*(B5), 2261, doi:10.1029/2002JB001787.
Saffer, D. M., and H. J. Tobin (2011), Hydrology and mechanics of subduction zone forearcs: Fluid flow and pore pressure, *Annu. Rev. Earth Planet. Sci.*, *39*, 157–186.
Sample, J. C. (1990), The effect of carbonate cementation of underthrust sediments on deformation styles during underplating, *J. Geophys. Res.*, *95*, 9111–9121, doi:10.1029/JB095iB06p09111.
Sample, J. C., and J. C. Moore (1987), Structural style and kinematics from an underplated slate belt Kodiak Island, Alaska, *Geol. Soc. Am. Bull.*, *99*, 7–20.
Schlunegger, F., and E. Kissling (2015), Slab rollback orogeny in the Alps and evolution of the Swiss Molasse basin, *Nat. Commun.*, *6*, 8605, doi:10.1038/ncomms9605.
Schmid, S. M. (1975), The Glarus overthrust: Field evidence and mechanical model, *Eclogae Geol. Helv.*, *68*, 247–280.
Schmid, S. M., B. Fügenschuh, E. Kissling, and R. Schuster (2004), Tectonic map and overall architecture of the Alpine orogen, *Eclogae Geol. Helv.*, *97*, 93–117.
Schwartz, S., and B. Stöckhert (1996), Pressure Solution in HP-LT metamorphic rocks—Constraints on the state of stress in deep levels of accretionary complexes, *Tectonophysics*, *255*, 203–209.
Seno, T. (2009), Determination of the fluid pressure ratio at seismogenic megathrusts in subduction zones: Implications for strength of asperities and Andean-type mountain building, *J. Geophys. Res.*, *114*, B05405, doi:10.1029/2008JB005889.
Simpson, G. (2014), Decoupling of foreland basin subsidence from topography linked to faulting and erosion, *Geology*, *42*, 775–778.
Sinclair, H. D. (1989), The North Helvetic flysch of eastern Switzerland: Foreland basin architecture and modeling, Ph.D. thesis, 119 pp., Univ. of Oxford.
Sinclair, H. D. (1997a), Tectonostratigraphic model for peripheral foreland basins. An Alpine perspective, *Geol. Soc. Am. Bull.*, *109*, 324–346.
Sinclair, H. D. (1997b), Flysch to molasse transition in peripheral foreland basins: The role of the passive margin breakoff, *Geology*, *25*, 1123–1126.
Sinclair, H. D., and P. A. Allen (1992), Vertical versus horizontal motions in the Alpine orogenic wedge: Stratigraphic response in the foreland basin, *Basin Res.*, *4*, 215–232.
Sinclair, H. D., B. J. Coakley, P. A. Allen, and A. B. Watts (1991), Simulation of foreland basin stratigraphy using a diffusion model of mountain belt erosion: An example from the Alps of eastern Switzerland, *Tectonics*, *10*, 599–620, doi:10.1029/90TC02507.
Strasser, M., et al. (2009), Origin and evolution of a splay fault in the Nankai accretionary wedge, *Nat. Geosci.*, *2*, 648–652.
Tichelaar, B. T., and L. J. Ruff (1993), Depth of seismic coupling along subduction zones, *J. Geophys. Res.*, *98*, 2017–2037, doi:10.1029/92JB02045.
Tobin, H., and D. M. Saffer (2009), Elevated fluid pressure and extreme mechanical weakness of a plate boundary thrust, Nankai Trough subduction zone, *Geology*, *37*, 679–682.
Trümpy, R. (1969), Die Helvetischen Decken in der Ostschweiz: Versuch einer palinspastischen Korrelation und Ansätze zu einer kinematischen Analyse, *Eclogae Geol. Helv.*, *62*, 105–142.
Tsuji, T., R. Kamei, and R. G. Pratt (2014), Pore pressure distribution of a mega-splay fault system in the Nankai Trough subduction zone: Insight into updip extent of the seismogenic zone, *Earth Planet. Sci. Lett.*, *396*, 165–178.
Park, J.–. O., T. Tsuru, S. Kodaira, P. R. Cummins, and Y. Kaneda (2002), Splay fault branching along the Nankai subduction zone, *Science*, *297*, 1157–1160.
Ujiie, K., and G. Kimura (2014), Earthquake faulting in subduction zones: Insights from fault rocks from accretionary prisms, *Prog. Earth Planet. Sci.*, *1*, 7, doi:10.1186/2197-4284-1-7.
Ujiie, K., A. J. Maltman, and M. Sánchez-Gómez (2004), Origin of deformation bands in argillaceous sediments at the toe of the Nankai accretionary prism, southwest Japan, *J. Struct. Geol.*, *26*, 221–231.
van de Kamp, P. (2008), Smectite-illite-muscovite transformations, quartz dissolution, and silica release in shales, *Clays Clay Miner.*, *56*, 66–81.
Vannucchi, P., and G. Bettelli (2002), Mechanisms of subduction accretion as implied from the broken formation in the Apennines, Italy, *Geology*, *30*, 835–838.
Wang, K. (1994), Kinematic models of dewatering accretionary prisms, *J. Geophys. Res.*, *99*, 4429–4438, doi:10.1029/93JB03366.
Wang, K., and Y. Hu (2006), Accretionary prisms in subduction earthquake cycles: The theory of dynamic Coulomb wedge, *J. Geophys. Res.*, *111*, B06410, doi:10.1029/2005JB004094.
Wiederkehr, M., R. Bousquet, M. A. Ziemann, A. Berger, and S. M. Schmid (2011), 3-D assessment of peak-metamorphic conditions by Raman spectroscopy of carbonaceous material: An example from the margin of the Lepontine dome (Swiss Central Alps), *Int. J. Earth Sci.*, *100*, 1029–1063.
Yamamoto, Y., H. Mukoyoshi, and Y. Ogawa (2005), Structural characteristics of shallowly buried accretionary prism: Rapidly uplifted Neogene accreted sediments on the Miura-Boso Peninsula, central Japan, *Tectonics*, *24*, TC5008, doi:10.1029/2005TC001823.